The Low-Resolution CCSM4

CHRISTINE A. SHIELDS, DAVID A. BAILEY, GOKHAN DANABASOGLU, MARKUS JOCHUM, JEFFREY T. KIEHL, SAMUEL LEVIS, AND SUNGSU PARK

National Center for Atmospheric Research, Boulder, Colorado

(Manuscript received 16 May 2011, in final form 16 December 2011)

ABSTRACT

The low-resolution version of the Community Climate System Model, version 4 (CCSM4) is a computationally efficient alternative to the intermediate and standard resolution versions of this fully coupled climate system model. It employs an atmospheric horizontal grid of 3.75° × 3.75° and 26 levels in the vertical with a spectral dynamical core (T31) and an oceanic horizontal grid that consists of a nominal 3° resolution with 60 levels in the vertical. This low-resolution version (T31x3) can be used for a variety of applications including long equilibrium simulations, development work, and sensitivity studies. The T31x3 model is validated for modern conditions by comparing to available observations. Significant problems exist for Northern Hemisphere Arctic locales where sea ice extent and thickness are excessive. This is partially due to low heat transport in T31x3, which translates into a globally averaged sea surface temperature (SST) bias of −1.54°C compared to observational estimates from the 1870–99 historical record and a bias of −1.26°C compared to observations from the 1986–2005 historical record. Maximum zonal wind stress magnitude in the Southern Hemisphere matches observational estimates over the ocean, although its placement is incorrectly displaced equatorward. Aspects of climate variability in T31x3 compare to observed variability, especially so for ENSO where the amplitude and period approximate observations. T31x3 surface temperature anomaly trends for the twentieth century also follow observations. An examination of the T31x3 model relative to the intermediate CCSM4 resolution (finite volume dynamical core 1.9° × 2.5°) for preindustrial conditions shows the T31x3 model approximates this solution for climate state and variability metrics examined here.

1. Introduction

As global climate models become increasingly sophisticated, so does the need for computing power and resources. Historically, the Community Climate System Model (CCSM) modeling community has supported several resolutions, including a computationally efficient lower-resolution version designed for applications requiring long integrations. (Boville and Gent 1998; Otto-Bliesner et al. 2002; Yeager et al. 2006). The latest CCSM release, CCSM, version 4 (CCSM4), is no different. This paper presents a low-resolution CCSM4 as an alternative to the higher resolution versions and highlights both its strengths and weaknesses in comparison with observations and other CCSM4 resolution versions.

CCSM4 contains several notable improvements spanning all model components, which include a much improved El Niño–Southern Oscillation (ENSO) representation, improved ocean mixing, a new land carbon–nitrogen (CN) component, more realistic ice albedos, and new coupling infrastructure. The low-resolution CCSM4 (henceforth called T31x3) uses a T31 spectral dynamical core for the atmospheric and land components (horizontal grid of 3.75° × 3.75°) with 26 atmospheric layers in the vertical. The ocean and ice components employ a nominal 3° irregular horizontal grid (referred to as x3) with 60 ocean layers in the vertical. The intermediate-resolution CCSM4 utilizes the finite-volume (FV) dynamical core (Lin 2004) with a nominal 2° atmosphere and land horizontal grid (1.9° × 2.5° latitude versus longitude) with 26 atmospheric layers in the vertical and a nominal 1° ocean and ice horizontal grid (referred to as x1) with 60 ocean layers in the vertical (henceforth called FV2x1). The standard CCSM4 resolution applies the finite-volume dynamical core with a 1° atmosphere (0.9° × 1.25° latitude versus longitude) with the same number of vertical levels coupled to the x1 ocean and ice models

Corresponding author address: Christine A. Shields, 1850 Table Mesa Drive, Boulder, CO 80305.
E-mail: shields@ucar.edu

DOI: 10.1175/JCLI-D-11-00260.1

(henceforth called FV1x1). Further details on CCSM4 model improvements and specifics about the higher resolution simulations can be found in Gent et al. (2011).

As indicated above, the low-resolution version of CCSM4 uses a spectral dynamical core rather than the finite-volume dynamical core used by other CCSM4 resolutions. Jablonowski and Williamson (2006) found that a low-resolution finite volume version (4° latitude versus 5° longitude) was too coarse to resolve baroclinic eddies and, thus, a major barrier to tropospheric climate studies. The minimum resolution necessary to sufficiently simulate storm systems with the finite-volume dynamical core is found to be 2.5° × 3.3° at nearly double the cost compared to T31 (P. Lauritzen 2011, personal communication). Although the finite-volume dynamical core may be optimal for tracer transport applications, including chemistry, given the need to provide the community with a computationally affordable alternative, the T31 spectral dynamical core was chosen for the atmosphere.

There are a number of physics differences in the T31x3 version of the model compared to the other CCSM4 resolutions. Minor cloud parametric changes (necessary to achieve radiative balance) are applied to the atmospheric component as well as the inclusion of a turbulent mountain stress (TMS) parameterization. Ice albedo and some ocean parameter settings are changed in the ice and ocean components, respectively. In the land component the ice melt runoff parameterization is not used. Here we present an overview of the simulations for each model component as well as review of the impact of resolution. Although all three CCSM4 resolutions are discussed in section 4, the majority of the paper places emphasis on the comparison between the low and intermediate resolutions of the model and comparisons to observation (section 5). Model variability, in particular, ENSO, the Northern Annular mode (NAM), and the Southern Annular Mode (SAM) are presented in section 6 along with a brief word on climate sensitivity in section 7. Finally, computational model performance statistics is presented to highlight the major cost savings associated with T31x3. This paper is not intended to be a comprehensive paper documenting all aspects of the T31x3 (or the FV2x1) simulation. Rather, it simply shows that the T31x3 is an alternative to the more costly FV2x1 by presenting a sample of basic climate state and variability metrics in comparison with available observations.

2. Model description and physics differences from standard CCSM4

CCSM4 is a fully coupled, global climate model consisting of atmosphere, land, ocean, and sea ice components as well as a coupler that passes state and flux information between the model components. A detailed description of the modeling system and each model component can be found in the *Journal of Climate* CCSM4 Special Issue Collection and includes papers by Gent et al. (2011) (overview), Neale et al. (2012, manuscript submitted to *J. Climate*) (atmosphere), Lawrence et al. (2012) (land), Danabasoglu et al. (2012) (ocean), Holland et al. (2012), and Jahn et al. (2012) (ice).

The atmosphere component is the Community Atmosphere Model, version 4 (CAM4) (Neale et al. 2012, manuscript submitted to *J. Climate*). Aside from the dynamical core differences discussed in the introduction, another important difference between the T31x3 and all other CCSM4 resolutions is the inclusion of the turbulent mountains stress (TMS) parameterization in CAM4, which significantly improves the coupled atmosphere–ocean interactions. TMS improves ocean surface stress in the low-resolution model and will be discussed further in sections 4 and 5. Although TMS was available in earlier versions of CAM, until now it has only been invoked within the Whole Atmosphere Community Climate Model (WACCM). TMS in WACCM was applied to better handle gravity waves in the upper atmosphere by improving the representation of subgrid-scale mountain ranges. Following the treatment of regular surface stress, CCSM4 assumes that the topography-induced roughness length is proportional to the standard deviation of subgrid topographic heights within the grid. The resulting neutral drag coefficient decreases linearly with stability. In the stable regime, the drag coefficient is down to zero where gradient Richardson number in the two lowest model layers is 1. Details about the origin of TMS parameterizations can be found in Klinker and Sardeshmukh (1992) and Milton and Wilson (1996). Another difference between the T31 version of CAM4 and the standard CAM4 is the adjustment of cloud process parameters. The relative humidity and autoconversion thresholds were slightly modified to achieve radiative top-of-atmosphere (TOA) balance for preindustrial conditions. Altering properties in the cloud parameterization scheme has been well documented in previous versions of CCSM (Yeager et al. 2006; Williamson et al. 1995; Hack et al. 2006) and continues to remain valid for CAM4. All resolution versions of CCSM4 include cloud parameter adjustments to achieve TOA balance and minimize drift in the coupled model.

The land component of CCSM4 is the Community Land Model, version 4 (CLM4) (Lawrence et al. 2012). Although there are no resolution-dependent physics differences, the T31x3 version of CCSM4 does not

account for the latent heat flux associated with snow and ice melt into liquid runoff. This is in contrast with the other resolution CCSM4 versions where the liquid and ice runoff amounts are kept track separately and the ocean model loses heat during the phase conversion from ice to liquid runoff. For the x3 ocean resolution, this approach created a problem in some isolated regions, for example, the Baffin Bay region where the ocean model continuously gets ice runoff and therefore continuously loses heat at the surface. Without adequate advective transport due to the coarse model grid, these cold regions stay local, leading to continuous ice formation with rather thick ice. Therefore, we chose to attain a more reasonable ice thickness at the expense of energy conservation in the released T31x3 model. The total runoff is always accounted for regardless of how ice runoff is treated. We also note that no CCSM version takes into account the temperature of the runoff water.

The CCSM4 ocean component is the Parallel Ocean Program version 2 (POP2) (Smith et al. 2010; Danabasoglu et al. 2012). The coarse-resolution configuration presented here uses the same nominal 3° horizontal grid described in Yeager et al. (2006) for CCSM3. However, the number of vertical levels has been increased from 25 levels in CCSM3 to 60 levels in the present x3 configuration. The associated vertical grid spacing is the same as the one employed in the x1 ocean model used in the standard CCSM4 version, thus allowing us to use the same prescriptions for the vertical mixing coefficients in all resolution versions. Due to this change in the vertical resolution, the discrete bottom topography was recreated using a smooth (one pass of a nine-point Gaussian filter) version of the 2-min gridded global relief data (National Oceanic and Atmospheric Administration 2006). As in the x1 version, the minimum and maximum ocean depths were set to 30 and 5500 m, and isolated holes were eliminated. Additional changes were then incorporated. These include Denmark Strait, Faroe Bank Channel, Weddell Sea, and Ross Sea overflow regions to accommodate the numerical requirements of an overflow parameterization as discussed in Danabasoglu et al. (2012). Furthermore, the Samoa Passage was widened to improve deep ventilation in the Pacific basin. Also, as in the x1 CCSM4 configuration, but in contrast with the x3 CCSM3, the Strait of Gibraltar was opened with a cliff topography to its immediate west to explicitly allow the Mediterranean overflow into the Atlantic basin.

All of the new physics developments and changes described in Danabasoglu et al. (2012) are used in the x3 configuration with the following differences from the x1 configuration: the upper-ocean lateral tracer diffusivity coefficients are increased to 4000 $m^2 s^{-1}$ (from 3000 $m^2 s^{-1}$) and the anisotropic horizontal viscosity coefficients are oriented along the model grid directions (instead of the east–west and north–south directions) with larger values. These larger viscosities are simply due to the coarser horizontal resolution of the x3 configuration. We note that there are three aspects of the horizontal viscosity formulation that are still the same between x3 CCSM3 and CCSM4 configurations: overall viscosity values, their grid-dependent orientations, and no dependency of these viscosities on the local deformation rate. The present x3 uses the same third-order upwind tracer advection scheme as in the x1 CCSM4 instead of the centered advection scheme of the x3 CCSM3. Finally, CCSM4 x3 now includes the parameterized diurnal cycle in shortwave heat flux unlike in the x3 CCSM3.

The CCSM4 sea ice component is based on the Community Ice Code version 4 (CICE4) (Hunke and Lipscomb 2008; Holland et al. 2012). Adjustments to ice albedos were required to simulate more reasonable ice extent and thickness values. Ice albedos designed for the x1 model are not appropriate for the low-resolution model and were decreased to compensate for excessive ice. In CCSM4, ice albedos are not adjusted directly but are computed using parameters representing optical properties of snow, bare sea ice, and melt ponds. These values are based on standard deviations from data obtained by the Surface Heat Budget of the Arctic (SHEBA) (Uttal et al. 2002).

3. Overview of simulations

Two T31x3 simulations are presented—a preindustrial control simulation (A.D. 1850 forcing) of 500 years in length and a modern twentieth-century transient simulation (A.D. 1850–2005 forcing). In sections 4 and 6, the T31x3 preindustrial simulation is compared to the FV2x1 preindustrial control as a means to show the viability of the T31x3 model as an alternative to the FV2x1 model. However, so as to evaluate the T31x3 model with respect to nature, in section 5, we analyze the modern period (1986–2005) of the twentieth-century simulation compared to observations. We will refer to the low-resolution preindustrial simulation as T31x3_1850, the low-resolution twentieth-century simulation as T31x3_20C, the intermediate and standard preindustrial simulations as FV2x1_1850 and FV1x1_1850, and the intermediate and standard twentieth-century simulations as FV1x1_20C and FV2x1_20C. Further details on FV1x1 and FV2x1 control and twentieth-century simulations can be found in Gent et al. (2011).

The T31x3_1850 control simulation was initialized using the Polar Science Center Hydrographic Climatology

dataset (PHC2) of potential temperature and salinity data [representing a blending of the Levitus et al. (1998) and Steele et al. (2001) data for the Arctic Ocean], and state of rest in the ocean model. The twentieth-century simulation was integrated for 150 years using aerosol, greenhouse gas, volcanic, solar, land use, and nitrogen deposition forcing suitable for the historical period of A.D. 1850–2005. This run was initialized from the T31x3_1850 control simulation at year 500. Unless otherwise stated, figures for mean state variables in this paper will use a 50-yr average taken from the end of each preindustrial control simulation and the last 20 years (1986–2005) for the twentieth-century simulations.

The decision was made to tune the T31x3 model to achieve a near zero TOA balance for 1850 conditions, in step with all other CCSM4 preindustrial control simulations (FV1x1_1850 and FV2x1_1850) documented in Gent et al. (2011). After tuning, the T31x3_1850 control simulation was integrated for 500 years but essentially came into a stable TOA radiative balance after 100 years of integration. The mean TOA heat imbalance computed using the last 50 years is $+0.09$ W m^{-2}. Following an initial, rapid decline, the ocean global volume-mean potential temperature, $\langle T \rangle$, increases almost linearly starting at year 50 (Fig. 1a). By the end of the 500-yr T31x3_1850 simulation, $\langle T \rangle$ is 3.80°C, representing a warming of about 0.10°C from its initial value. The oceanic heat gain remains rather steady at 0.16 W m^{-2} ($=$0.11 W m^{-2} when scaled by the entire surface area of the earth) after the initial transient and largely reflects the TOA heat gain of 0.09 W m^{-2} in the coupled system. In comparison with the initial condition, most of this heat gain occurs in the 500–3500-m depth range while the ocean loses heat above 500-m depth (not shown). We note that the heat gain in T31x3_1850 is in stark contrast with both FV1x1_1850 and FV2x1_1850 in which the ocean actually loses heat at -0.14 W m^{-2} (over the last 700 years) and -0.09 W m^{-2} (over the last 600 years), respectively. The ocean global volume-mean salinity, $\langle S \rangle$, shows a small, but linear freshening trend after year 50, corresponding to -2.9×10^{-4} psu century^{-1} for years 50–500 (Fig. 1b). Nevertheless, due to the initial salt gain, $\langle S \rangle$ at year 500 is only 4×10^{-4} psu fresher than its initial value. Similar freshening with comparable trends is also seen in FV1x1_1850, while FV2x1_1850 does not show any monotonic and discernable trends in $\langle S \rangle$.

An important metric for a coarse-resolution coupled model is to have a stable meridional overturning circulation, particularly in the Atlantic basin (Yeager et al. 2006). We show the Atlantic meridional overturning circulation (AMOC) maximum transport time series from T31x3_1850 in Fig. 1c. Here the maximum transport is searched for below 500-m depth between 30° and 60°N, and it includes parameterized eddy contributions in addition to the mean flow. Following an initial decline, the model maintains a robust AMOC with a mean maximum transport of 17.4 Sv (Sv $\equiv 10^6$ m^3 s^{-1}) over the last 100 years. This transport, however, is smaller than in both FV1x1_1850 (~26 Sv) and FV2x1_1850 (~26 Sv and ~23 Sv in high and low transport regimes, respectively).

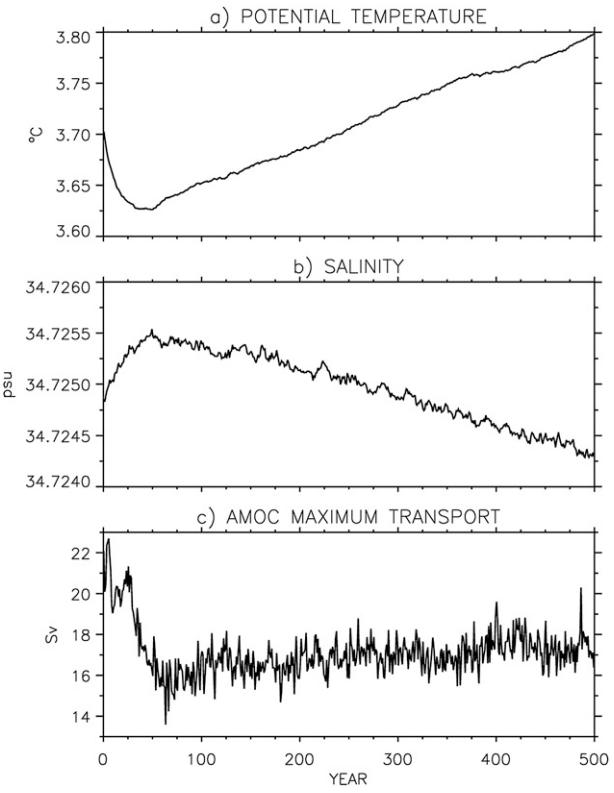

FIG. 1. Annual-mean time series of (a) global volume-mean potential temperature, (b) global volume-mean salinity, and (c) Atlantic meridional overturning circulation (AMOC) maximum transport for T31x3_1850. The AMOC maximum is searched for below 500-m depth between 30° and 60°N and it includes the mean flow and parameterized eddy contributions.

4. Resolution differences

a. Ocean SST and zonal wind stress

The T31x3_1850 sea surface temperature (SST) difference distribution from the Hurrell et al. (2008) dataset is presented in Fig. 2 in comparison with the FV1x1_1850 and FV2x1_1850 differences from the same observational data. For these preindustrial comparisons, the observational estimate is based on the 1870–99 time-mean SST. In T31x3_1850, the global-mean SST bias is -1.54°C, colder than in both higher resolution versions.

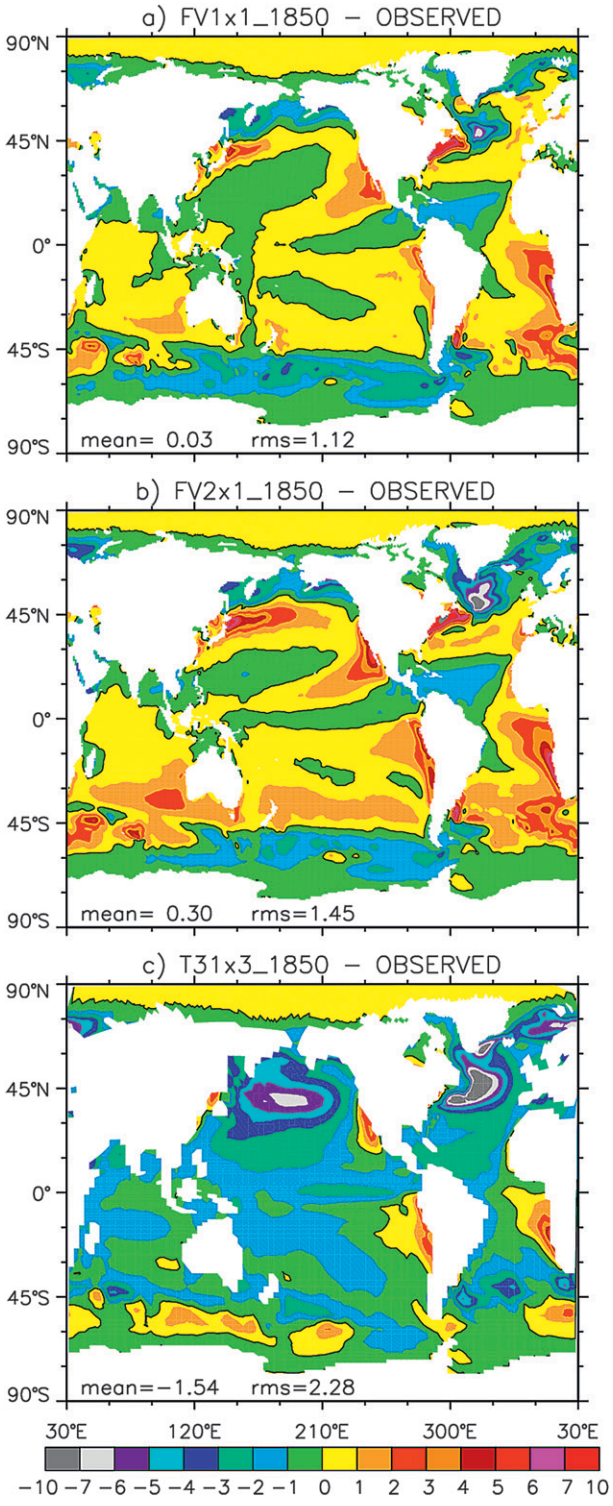

FIG. 2. Model SST differences (°C) from the Hurrell et al. (2008) observational data for (a) FV1x1_1850, (b) FV2x1_1850, and (c) T31x3_1850. The 1870–99 time-mean SST is used for observations. The mean and rms differences from observations are also given.

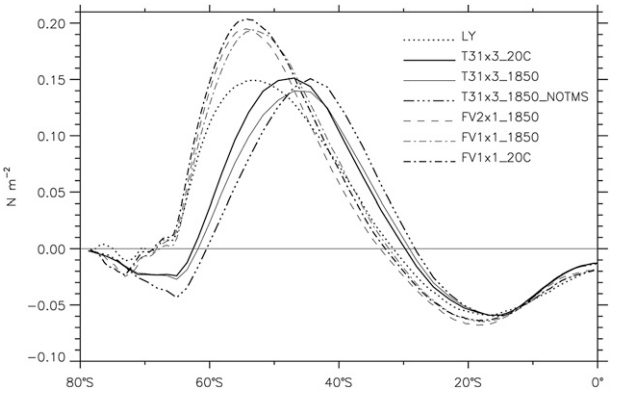

FIG. 3. Zonal-mean zonal wind stress. LY represents an estimate based on the Large and Yeager (2009) dataset.

The root-mean-square difference of 2.28°C from observations in T31x3_1850 also represents the largest departure from observations among these control cases. The warm bias magnitudes in the upwelling regions off the west coast of South America, South Africa, and California are comparable in T31x3_1850 and FV1x1_1850—in both, these biases are smaller than in FV2x1_1850. The largest cold biases in excess of 6°C occur in the North Pacific and North Atlantic in T31x3_1850. These are due to more southerly paths of the Kuroshio and Gulf Stream/North Atlantic Currents and subsequent penetration of the subpolar gyres too far south in both basins, and they are noticeably different than those of FV1x1_1850 and FV2x1_1850. These differences primarily reflect changes in the barotropic circulation, partly resulting from differences in the wind stress curl fields that largely determine the interior gyre circulation through the Sverdrup balance in these coarse resolution simulations (Danabasoglu 1998). In particular, the T31x3_1850 wind stress curl exhibits a subpolar positive pattern with significantly more southward excursion than in FV1x1_1850 and FV2x1_1850 (not shown).

Zonal averages of the zonal wind stress component from preindustrial and twentieth-century simulations for the Southern Hemisphere are presented in Fig. 3 (discussion of the twentieth-century results is deferred to section 5b). Both preindustrial simulations with the FV dynamical core show very similar distributions with similar maximum wind stresses (>0.19 N m^{-2}) located at about 54°S, indicating little sensitivity to the horizontal resolution of the atmospheric model. In comparison, the Southern Hemisphere storm track is displaced farther north and its maximum strength is smaller (0.14 N m^{-2} located at 47°S) in T31x3_1850. The TMS parameterization appears to contribute to this weakened wind stress as a sensitivity simulation (referred

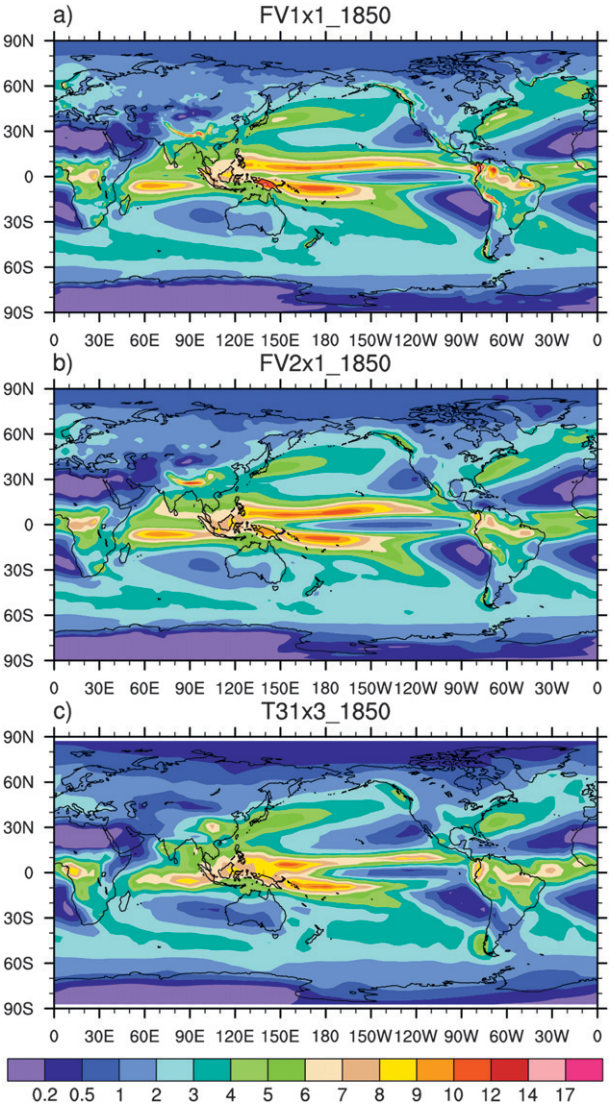

FIG. 4. Annually average precipitation rate (mm day^{-1}) for (a) FV1x1_1850, (b) FV2x1_1850, and (c) T31x3_1850.

to as T31x3_1850_NOTMS in Fig. 3) shows roughly 10% larger magnitudes without it.

b. *Precipitation and river transport*

Annual-averaged precipitation rate across different model horizontal resolutions (Fig. 4) is shown for the 1850 control runs. All three resolutions exhibit the signature double intertropical convergence zone also seen in CCSM3 (Hack et al. 2006) and previous versions of the model, regardless of dynamical core. In general, the precipitation rate and precipitable water (not shown) are reduced in T31x3 compared to both FV2x1 and FV1x1 as evidenced by a globally averaged value of 2.64 mm day^{-1} of precipitation rate for T31x3 as opposed to 2.93 and 2.87 for FV2x1_1850 and FV1x1_1850, respectively. Spatially, this can be seen in Fig. 4 with the largest differences in the tropical Pacific. In part, this can be attributed to the fact that the T31x3 is a colder model (Figs. 2 and 8) than its higher resolution counterparts, so less precipitable water is available to the system. Less precipitation improves the comparison to observations in the twentieth-century run (discussed in section 5a), which in turn improves sea surface salinity biases (section 5c).

River flow acts as an integrator of processes across river basins. Such processes include mass and energy exchange at the land–atmosphere interface, in the soil, and in plants. Gent et al. (2010) evaluated 2° and 0.5° preindustrial simulations of the CCSM3.5 by analyzing the river flow simulated by the CLM river transport model. Gent et al. found improved river flow at higher resolution and attributed this mainly to the improved simulation of atmospheric variables in CAM and, to a lesser degree, the improved representation of land surface processes, such as snow cover, in the CLM. Following a similar approach here, we assess whether the T31x3_1850 simulation shows degraded river transport relative to the FV2x1_1850 simulation. For the most part, it does not. Cumulatively, the T31x3 model underestimates, and the FV2x1 and FV1x1 models overestimate, freshwater input to the Northern Hemisphere oceans relative to observational estimates (Dai and Trenberth 2002) (Fig. 5a). The FV2x1_1850 model is in closer agreement to the global total observed runoff, partly due to compensating biases. The T31x3_1850 model performs better than the FV2x1_1850 in the Atlantic Ocean basin (Fig. 5b) and better than both FV models in the Indian Ocean basin (Fig. 5c), although the T31x3_1850 model underestimates runoff in the northern Indian Ocean. In the Pacific Ocean basin it is more difficult to pick the better simulation (Fig. 5d). These changes can be attributed to increased precipitation in the T31x3_1850 simulation in the Amazon Basin and near the 30°–40°N latitude band and decreased precipitation in monsoon regions surrounding the Indian Ocean (Fig. 4). The T31x3_1850 model shows a sharp reduction in Arctic runoff relative to the FV models (Fig. 5e) due to a strong high-latitude cold bias at T31x3 (Figs. 2 and 8). Colder temperatures are accompanied with reduced precipitation (Fig. 4). Colder temperatures also lead to the accumulation of water in perennial soil ice (not shown).

c. *Sea ice and northward heat transport impact*

A key result when analyzing sea ice across resolutions (Fig. 6) is that the ice extent in the Arctic improves with resolution. This is mostly due to an improvement in the Northern Hemisphere winds (not shown) and atmospheric and oceanic heat transport with resolution. Note

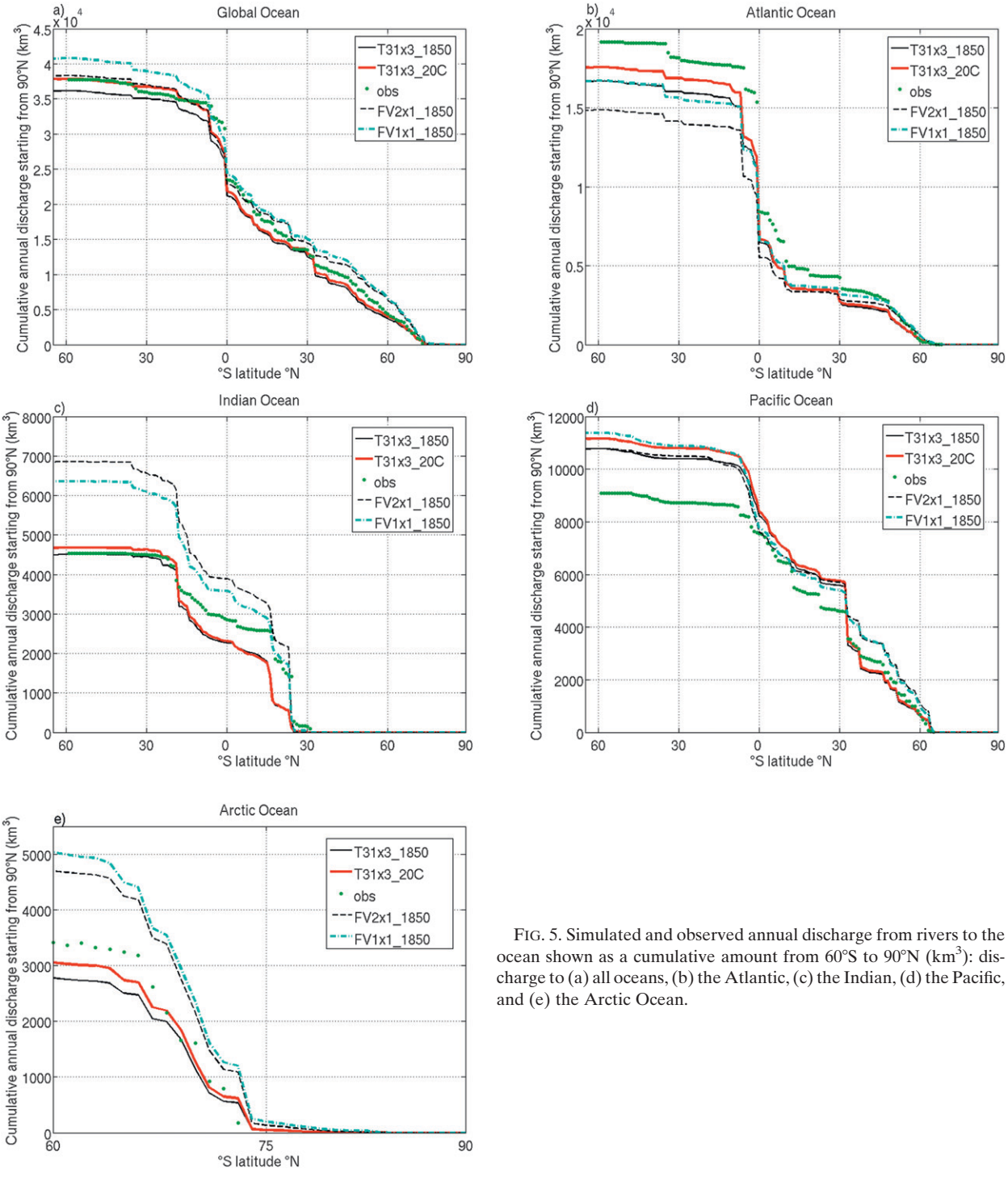

FIG. 5. Simulated and observed annual discharge from rivers to the ocean shown as a cumulative amount from 60°S to 90°N (km^3): discharge to (a) all oceans, (b) the Atlantic, (c) the Indian, (d) the Pacific, and (e) the Arctic Ocean.

that the sea ice is too extensive in both T31x3 and FV2x1 simulations in boreal winter (Fig. 6, upper panels) compared to the Special Sensor Microwave Imager (SSM/I) satellite observations (Cavalieri et al. 1996) (solid black line) and by contrast well simulated in the FV1x1 simulation. When evaluating sea ice extent time series across the entire length of the 1850 control simulations, we find that the FV2x1 simulation produces a sea ice pattern in the Labrador Sea very similar to FV1x1 (not shown) during some time periods, while most time periods exhibit a spatial extent as seen in Fig. 6. In both T31x3 and FV1x1, the sea ice extent is stable and

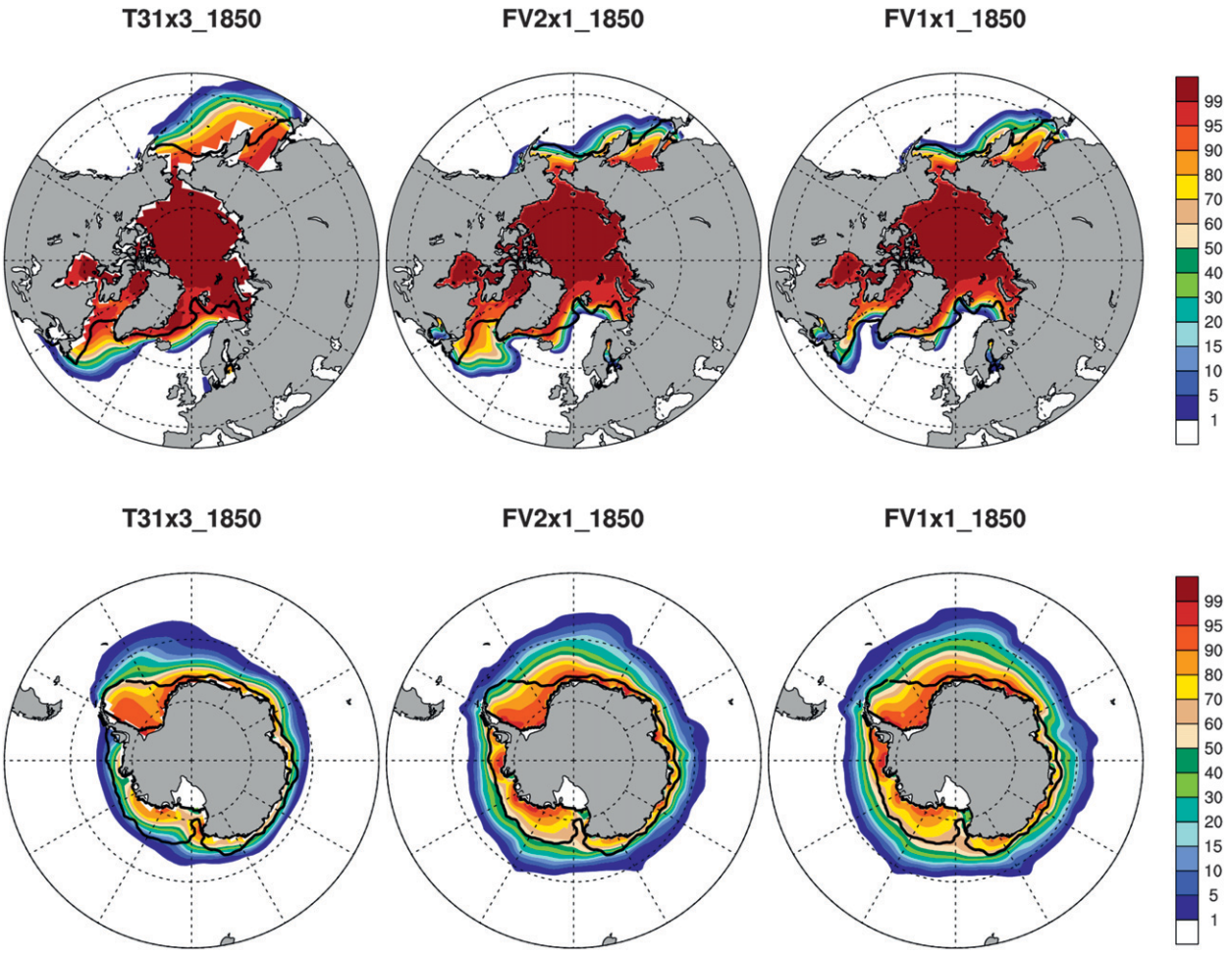

FIG. 6. Sea ice fraction (%) for T31x3_1850, FV2x1_1850 and FV1x1_1850 in (top) Northern Hemisphere JFM (boreal winter) and (bottom) Southern Hemisphere JFM (austral summer). SSM/I observations for sea ice 10% concentration are shown with a heavy black line for reference.

similar across all years in the control experiments. The Southern Hemisphere sea ice area is shown in Fig. 6 (lower panels). The austral summer [January–March (JFM)] minimum extent and area in the T31x3_1850 simulation are closer to SSM/I satellite observations (Fig. 6, lower panels) than either of the higher resolution versions. Similarly, the sea ice is thinner overall in T31x3_1850 and more in agreement with the sparse observational estimates of Southern Hemisphere sea ice thickness (not shown).

The relatively poor performance of the model in representing the Northern Hemisphere sea ice compared to Southern Hemisphere sea ice is due to different processes. In the Northern Hemisphere it is accomplished by coastal boundary currents, which are neither resolved nor parameterized. This leads to a too small poleward heat transport in the Arctic. With higher resolution, resolving these coastal currents leads to a redistribution of heat and a reduced sea ice bias in the Northern Hemisphere (Jochum et al. 2008). In the Southern Hemisphere the sea ice distribution becomes worse with higher resolution due to the fact that the Southern Hemisphere westerlies are overly strong (Holland and Raphael 2006). Why these westerlies become stronger and worse as the resolution increases is an open question since Boville (1991). Bitz et al. (2005) also discusses important factors in determining ice extent in observations and models.

These concepts are nicely demonstrated in the various CCSM4 simulations. Poleward heat transport in the x3 ocean is lower than both observationally based estimates and the higher resolution simulations in the Northern Hemisphere while similar to the x1 ocean in the Southern Hemisphere (see Fig. 15). This is also true of the northward heat transport by the atmosphere (not shown). The magnitude of the Southern Hemisphere wind stress in the x3 ocean compares better to observational estimates than

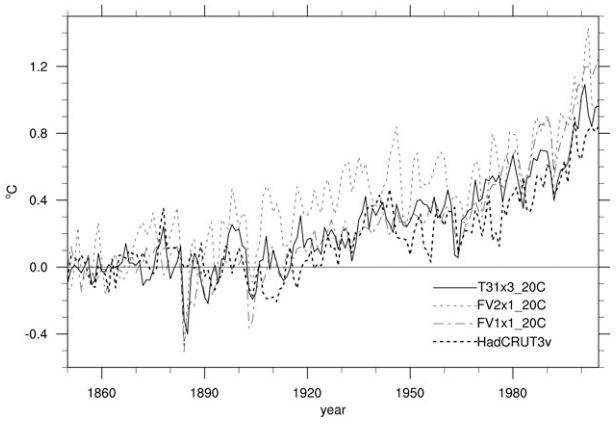

FIG. 7. Annual-mean time series of globally averaged surface temperature anomaly from HadCRUT3v data (Brohan et al. 2006). FV1x1 is an ensemble mean, and FV2x1 and T31x3 are single realizations. Anomalies are computed relative to the mean of the first 20 years of each time series.

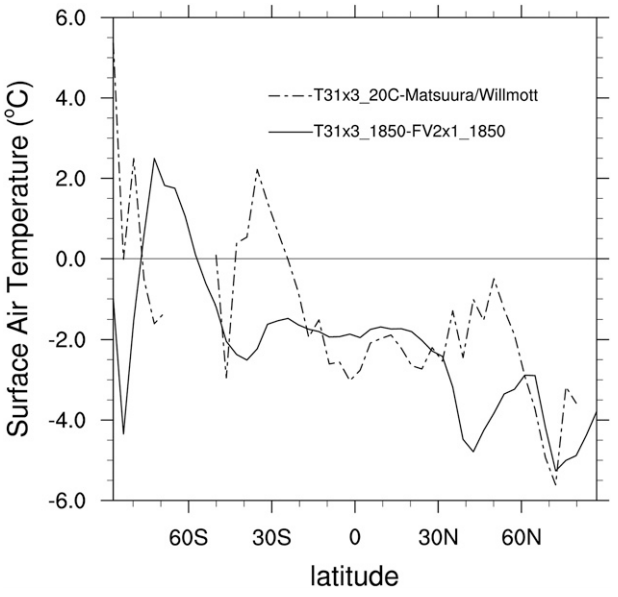

FIG. 8. Annually averaged surface air temperature zonal average differences. The dashed line shows surface air temperature over land for T31x3_20C minus observations. Observations are derived from the Matsuura and Willmott (2009) air temperature time series. Climatology was computed using years 1950–99. Solid line shows surface air temperature globally for T31x3_1850 minus FV2x1_1850. The zero line is marked for reference.

the higher resolution models, which are all too high (Fig. 3). The equatorward displacement of the wind stress in the x3 ocean is corrected somewhat by inclusion of the TMS parameterization (Fig. 3). It is important to note that neither the intermediate nor standard resolution experiments apply TMS. Given that the Southern Hemisphere poleward heat transport is similar at all resolutions, the likely explanation for the improvement in Antarctic sea ice extent is due to the improvement in wind stress. In the Northern Hemisphere, the weak northward heat transport in the atmosphere and ocean explains the thicker and more extensive sea ice in the low resolution CCSM4. Other work (C. Bitz 2011, personal communication) on the ultrahigh-resolution CCSM4 shows a high bias in northward heat transport (atmosphere and ocean). Consequently, in the Northern Hemisphere, sea ice is too thin and the extent too low, while the Southern Ocean extent is similar to other resolutions due to a similar bias in the surface wind stress.

d. Twentieth-century surface temperature anomalies

When comparing the twentieth-century simulations across resolutions, surface temperature anomalies are examined. Anomalies are computed using the mean of the first 20 years of each case (Fig. 7) following Gent et al. (2011). The T31x3 time series tracks closely with the observational record [the Hadley Centre and Climate Research Unit (at the University of East Anglia) gridded near-surface temperature dataset (HadCRUT3v)] and the FV1x1_20C. The FV2x1_20C is an outlier in that the surface temperature anomalies are greater than observed. By the end of the twentieth-century period, the T31x3 anomalies compare more closely to the observations than either the FV2x1_20C or the FV1x1_20C anomalies, yet are still slightly biased high. This result is consistent with Gent et al. (2011), which shows the CCSM4 response to the late twentieth-century historical forcing to be too strong.

5. Climate state and comparison to observations

a. The atmosphere and land solutions

There are a number of systematic biases in the atmospheric simulation that are documented here. The bias in simulated annual, zonal-mean land surface air temperature is shown in Fig. 8. For the twentieth-century simulation, the simulated surface air temperature is too cold (by 2°–5°C) compared to the observations. The cold surface air temperature bias in the tropical regions is related to a deficit of incoming shortwave radiation in this region (not shown), where the energy deficit is as large as 30–40 W m^{-2} in certain regions. At higher Northern Hemisphere latitudes, the cold bias in the model is related to weak ocean heat transport (see Fig. 15) compared to observations. Figure 8 also indicates that the T31X3_1850 simulation is significantly colder over most latitudes than the FV2X1_1850 simulation, which is again indicative of biases in both the simulated surface energy budget and weak poleward heat transport in the T31X3 model.

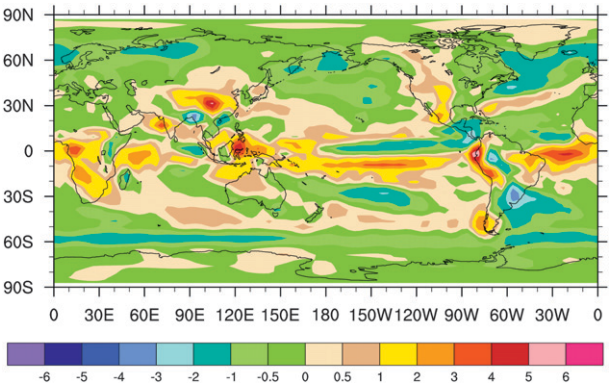

FIG. 9. Annually averaged precipitation difference for T31x3_2000 from GCPC observations (mm day^{-1}).

To further investigate the role of biases in surface energy and ocean heat transport, a sensitivity study was carried out to test whether addressing the tropical surface energy bias could lead to an improvement in overall meridonal surface air temperatures. The regional bias in absorbed shortwave energy in the tropical Atlantic ranges from 30 to over 40 W m^{-2}, whereas the model underestimates shortwave energy absorbed at the ocean surface. One hypothesis is that this under representation of shortwave energy at the surface is linked to high-latitude cold surface temperatures because this missing tropical energy is not available to be transported to higher latitudes. To test this hypothesis, cloud properties were tuned to allow more shortwave radiation to reach the tropical surface, thus forcing the model to agree better with observational estimates of the surface shortwave budget (to locally within 10 W m^{-2} of observations). The tropical surface air temperatures from this retuned model did increase (in fact, they were too warm compared to observational estimates by over 2°C), but high-latitude temperatures remained too cold compared to observations, similar to the control version of the model. This result indicates that, even if one were to improve the local shortwave bias in the tropical surface energy budget, the x3 ocean model cannot efficiently transport this heat poleward to reduce the cold bias at high latitudes (see Fig. 15).

The bias in twentieth-century simulated annual mean precipitation (Fig. 9) illustrates the signature of a double-ITCZ structure in the tropical Pacific, which exists in all resolution versions (Fig. 4.) Although the T31x3 compares to other resolutions, regional biases specific to the low-resolution version certainly exist. There is a significant bias in the location of the maxima in the Indian monsoon (seen in June–August), where more precipitation occurs in the Arabian Sea region compared to the Bay of Bengal. There is also excessive precipitation in the western Pacific warm pool region leading to low salinities in this region (see Fig. 13). Precipitation in the Congo region is also a significantly overestimated, which correlates through enhanced runoff with a low salinity bias in the southern Atlantic coastal region off of Africa (see Fig. 13).

The T31X3_20C zonal annual mean atmospheric temperature structure has many realistic features compared to reanalysis (Kalnay et al. 1996) as shown in Fig. 10. The comparison (Fig. 10c) shows the well-known bias signature of a cold polar upper troposphere of magnitude 7° to 8°C, a feature that has existed in previous versions of the CCSM regardless of resolution, (Collins et al. 2006; Neale et al. 2012, manuscript submitted to *J. Climate*). The atmosphere, in general, is too cold compared to the reanalysis. Comparison with other reanalysis products and satellite data (not shown) confirm this general feature of the model. The tropical tropopause region also is too cold by ~7°C, which will affect the model's ability to simulate realistic stratospheric water vapor.

The T31X3_20C annually averaged zonal mean wind is shown in Fig. 11. Note that in the Southern Hemisphere the jet is displaced too far equatorward, which is reflected in the bias in the zonal surface stress (Fig. 3). The equatorward displacement of the jets is a signature of the low-resolution model. With increased horizontal resolution the Southern Hemisphere jet strengthens and shifts poleward.

The simulated Northern Hemisphere 500-hPa height field is compared to reanalysis in Fig. 12. The T31X3_20C simulation of the Pacific Northwest ridge is in better agreement than the higher resolution simulations (not shown). This improvement may be due to to the TMS parameterization, but also could be related to the position of tropical Pacific heating given that this ridge is related to Rossby wave propagation from the central Pacific region. The biases in the simulated height field of the North Atlantic region points to biases in the Arctic circulation that exacerbate biases in Arctic sea ice thickness and extent (see Figs. 6 and 16).

Finally, for land model diagnosis, we evaluate river discharge as in section 4. Here we add the T31x3_20C simulation to the comparison shown in Fig. 5. We find that in all ocean basins except the Pacific the T31x3_20C simulation performs similar to or better than the three 1850 configurations relative to the observations. This statement holds primarily for the cumulative ocean basin discharge values and is reassuring considering that the observations correspond to the present day.

b. *The ocean solution*

The SST and sea surface salinity (SSS) differences from the present-day Hurrell et al. (2008) dataset (1986–2005

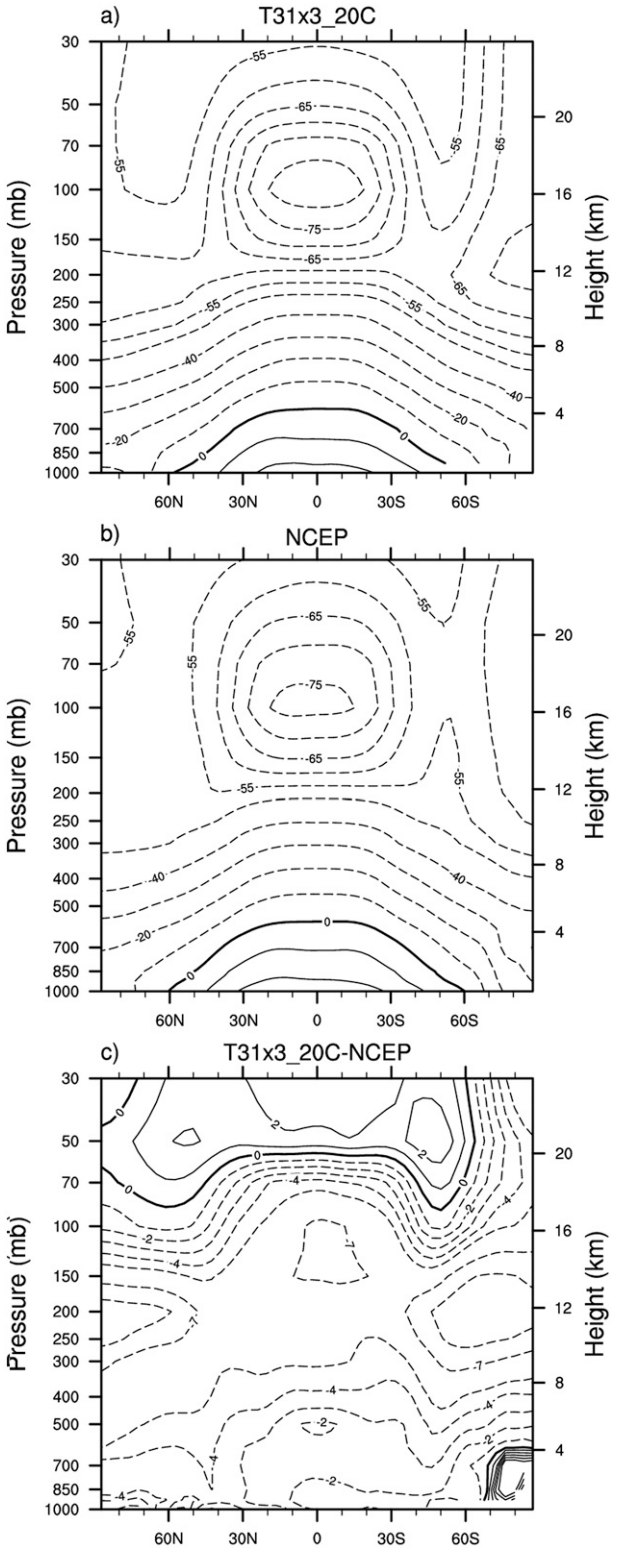

FIG. 10. Annually averaged zonal mean air temperature (°C) with height for (a) T31x3_20C, (b) NCEP reanalysis, and (c) their difference. Contour intervals for (a),(b) are every 5 degrees from −85°C through −50°C with all subsequent contours every 10°C; contour intervals for (c) are −9, −7, −5, −4, −3, −2, −1, 0, 1, 2, 3, 4, 5, 7, and 9. Solid (dashed) lines are positive (negative) values.

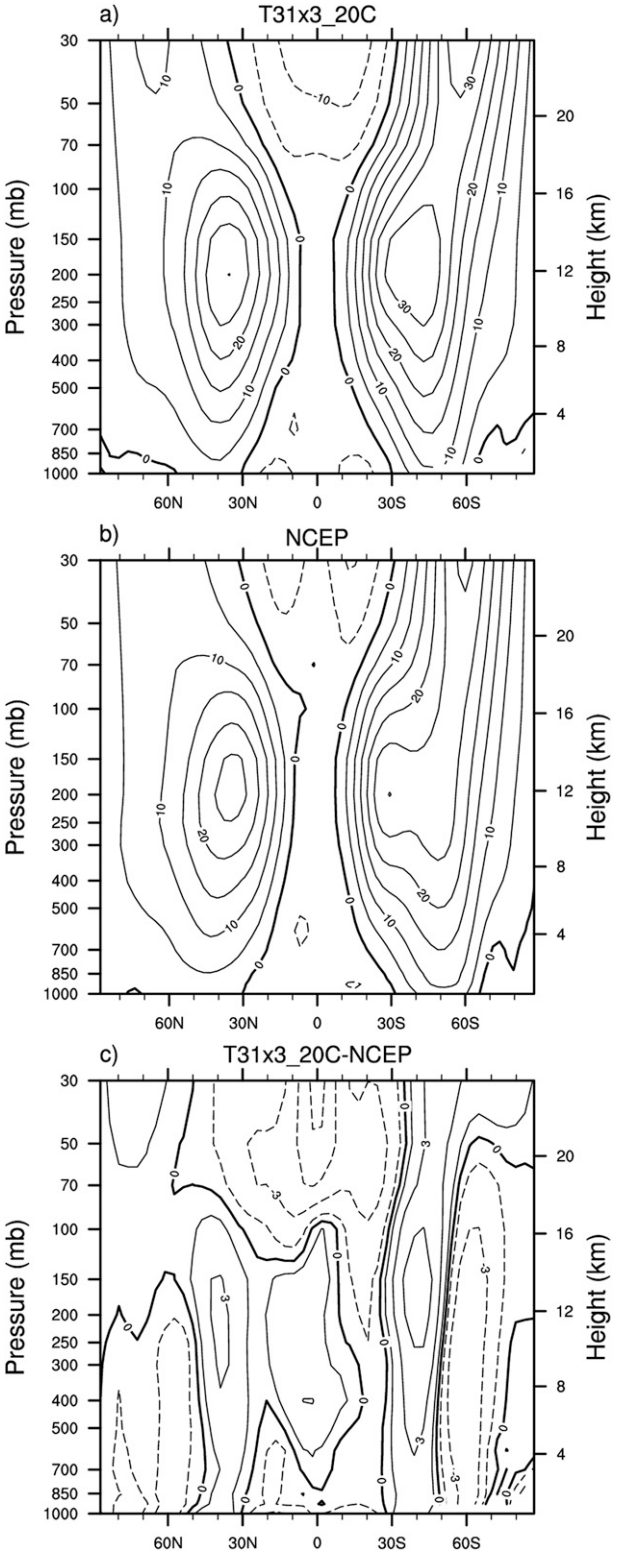

FIG. 11. Annually averaged mean zonal wind (m s^{-1}) with height for (a) T31x3_20C, (b) NCEP reanalysis, and (c) their difference. Contour intervals for (a),(b) are every 5 m s^{-1} from −20 to 30 m s^{-1} with all subsequent contours 10 m s^{-1}; contour intervals for (c) are −18, −15, −12, −9, −6, −3, 1, 0, 1, 3, 6, 9, 12, 15, and 18. Solid (dashed) lines are positive (negative) values.

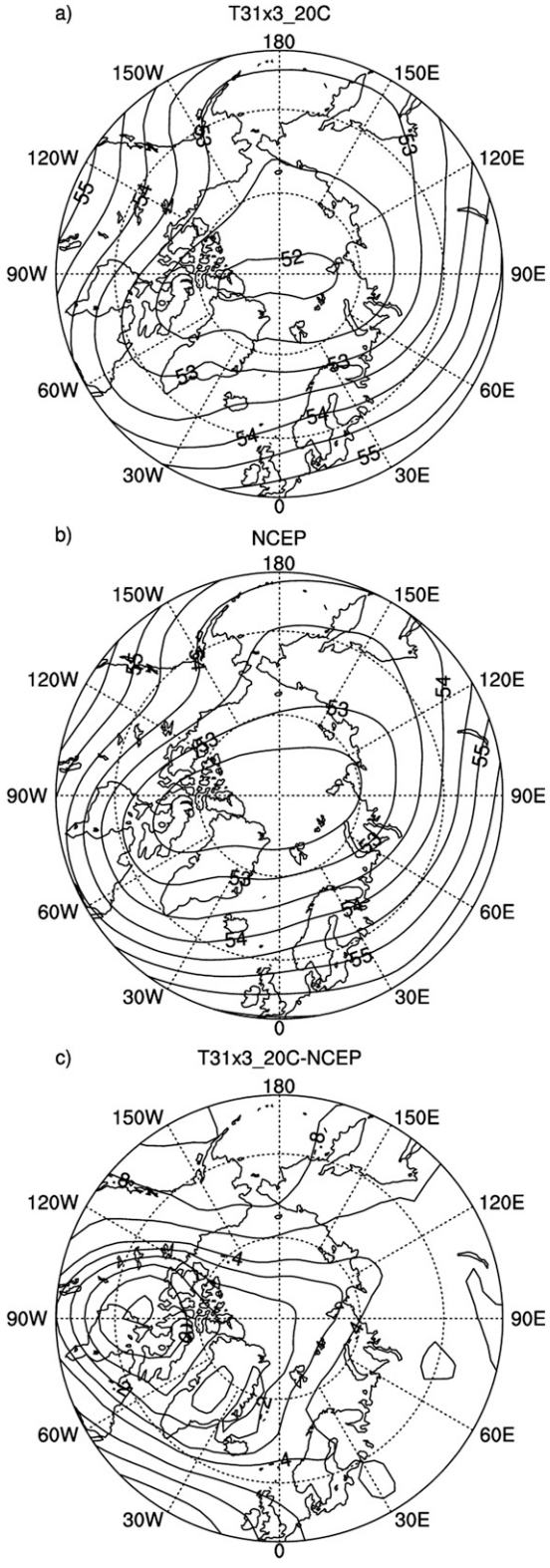

FIG. 12. Annually averaged 500-hPa geopotential height [hectometers (hm)] for (a) T31x3_20C, (b) NCEP reanalysis, and (c) their difference. Contour intervals for (a),(b) are every 0.5 hm and for (c) are −1, −0.8, −0.6, −0.4, −0.3, −0.2, −0.1, 0, 0.1, 0.2, 0.3, 0.4, 0.6, 0.8, and 1 hm.

mean) and the Polar Science Center Hydrographic Climatology (PHC2) [a blending of the Levitus et al. (1998) and Steele et al. (2001) data for the Arctic Ocean], respectively, are shown from T31x3_20C in Fig. 13. The global-mean SST is colder than in observed by −1.26°C, and the associated rms difference is 1.88°C. These can be contrasted with the corresponding FV1x1_20C values of 0.30° and 1.14°C. The present-day SST difference patterns and most magnitudes are very similar to those of the preindustrial control simulation (Fig. 2c). The largest exception is the reduced cold bias in the North Pacific. The SSS difference distribution shows a substantial reduction of the fresh bias in T31x3_20C compared to FV1x1_20C with mean biases of −0.15 and −0.37 psu, respectively. The rms error in T31x3_20C (0.94 psu) is very similar to that of FV1x1_20C (0.88 psu). We believe that the reduced fresh bias in T31x3_20C largely reflects the improvements in precipitation with much reduced mean and rms errors compared to observations than in the higher resolution versions.

The AMOC remains rather robust throughout T31x3_20C with its maximum transport fluctuating roughly between 15.5 Sv and 19.5 Sv (not shown). As in the FV1x1_20C simulations, the maximum transport diminishes only slightly by 1–2 Sv toward the end of the twentieth century. For this later period (1986–2005), Fig. 14 presents the time-mean global and Atlantic MOC distributions for the total flow, showing generally weaker transports in T31x3_20C than in both the higher resolution versions and available observations. For example, the cell associated with the North Atlantic Deep Water (NADW, large clockwise circulation in the Northern Hemisphere in both panels) has a maximum transport of 16.8 Sv, smaller than the FV1x1_20C transport of 24 Sv. At the latitude of the RAPID observations (26.5°N), the AMOC maximum transport is about 13.5 Sv, lower than the observational mean transport estimate of 18.7 Sv (Cunningham et al. 2007). In T31x3_20C the combined Denmark Strait and Faroe Bank Channel overflow transport is also low, that is, 3 Sv compared to available observational estimates (6.4–9.4 Sv) and that of the FV1x1_20C (5.2 Sv). Despite the parameterized overflows, the penetration depth of the NADW remains shallow. Here, this depth is defined as the depth of the zero contour line, separating the NADW cell from that of the Antarctic Bottom Water (AABW, counterclockwise circulation below about 3000-m depth in Fig. 14b). Indeed, while the RAPID observations show about 4350 m as the NADW penetration depth at 26.5°N, T31x3_20C penetration depth is only 3250 m, more than 1000 m shallower. Such shallow NADW penetration depths appear to be a common feature of other CCSM4 simulations owing to coupled

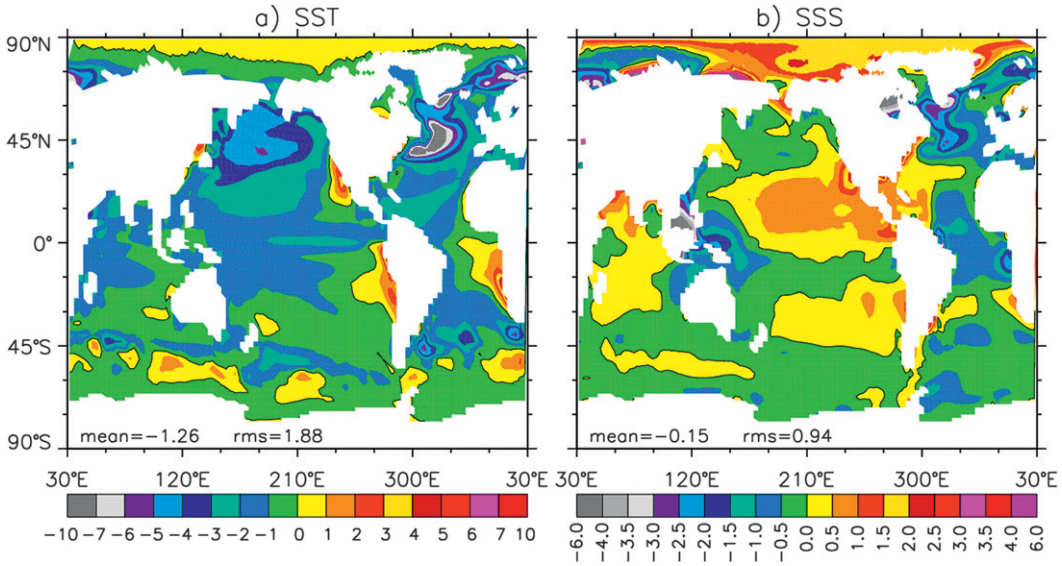

FIG. 13. Sea surface (a) temperature (°C) and (b) salinity (psu) T31x3_20C minus observations difference distributions. For temperature and salinity, the Hurrell et al. (2008) and PHC2 datasets are used, respectively.

model density biases in the North Atlantic, as discussed in detail in Danabasoglu et al. (2010) and Danabasoglu et al. (2012). Finally, the transport associated with the AABW is weaker in T31x3_20C (>4 Sv global) than in both FV1x1_20C (>8 Sv global) and the range of observational estimates. We refer to Danabasoglu et al. (2012) for further discussion on MOC.

In FV1x1_20C, the model deep-water formation sites in the North Atlantic include the Labrador Sea basin, in good agreement with observational estimates of deep convection sites. Unfortunately, this improvement is absent in T31x3 simulations where the main deep convection site is located just south of Iceland (not shown). Furthermore, both the geographical extent of the region with, for example, mixed layer depths (MLDs) > 250 m, and the mean maximum MLD are much smaller in T31x3_20C than in FV1x1_20C. These MLD changes along with weaker NADW transport cannot be attributed to coupled model biases as they are also present in forced ocean-only simulations at this resolution. An in-depth analysis of the ventilation and mixing properties of the x3 ocean simulation in comparison with those of the x1 simulations and observations is conducted in a complementary study (K. Moore 2012, personal communication).

We show the global and Atlantic Ocean total northward heat transports (NHTs) from T31x3_20C in comparison with those of FV1x1_20C and the implied transport estimates from Large and Yeager (2009) based on the observationally based surface flux data for the 1984–2006 period in Fig. 15. An Atlantic Ocean estimate using the RAPID data from Johns et al. (2011) is also included. As in the CCSM3 low-resolution version, NHT in the Atlantic Ocean is lower than either the implied estimate or in FV1x1_20C. The peak transport reaches only 0.66 PW located between 17° and 23°N. The ocean model is likely responsible for this deficiency that accompanies weaker AMOC because forced ocean-only simulations produce similar or slightly larger NHT in the Atlantic basin. The global NHT however remains closer to the implied estimate range owing to a larger contribution from the Pacific domain. While the FV1x1_20C and T31x3_20 NHTs are almost the same with similar departures from the implied estimate between 15°S and 10°N, the NHT in T31x3_20C compares more favorably with the implied estimate than in FV1x1_20C south of 15°S.

The zonal-mean zonal wind stress maximum of 0.15 N m^{-2} in T31x3_20C is in excellent agreement with the estimate from Large and Yeager (2009) (Fig. 3). However, the model shows an unrealistic migration of the Southern Hemisphere storm track toward the equator, as in the low-resolution preindustrial simulation. Due to this northward shift, the Antarctic Circumpolar Current transport at Drake Passage is only 105 Sv, lower than the Cunningham et al. (2003) observational estimate of 137 ± 8 Sv. In FV1x1_20C, while the latitude of the maximum zonal-mean zonal wind stress is in agreement with the Large and Yeager (2009) data, its magnitude is >30% larger.

The larger lateral viscosities required by the model's low horizontal resolution produce wider western boundary currents with generally smaller transports compared to

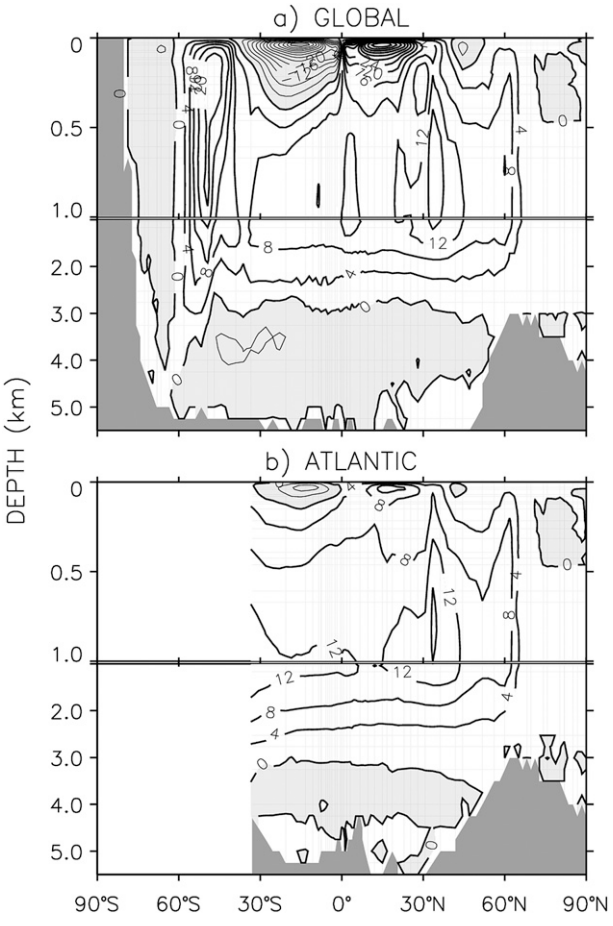

FIG. 14. Meridional overturning circulation (Sv) for (a) global and (b) Atlantic Oceans from T31x3_20C. The plots represent the total overturning circulation that include the Eulerian-mean and parameterized mesoscale and submesoscale contributions. The positive and negative (shaded regions) contours denote clockwise and counterclockwise circulations, respectively: contour interval 4 Sv.

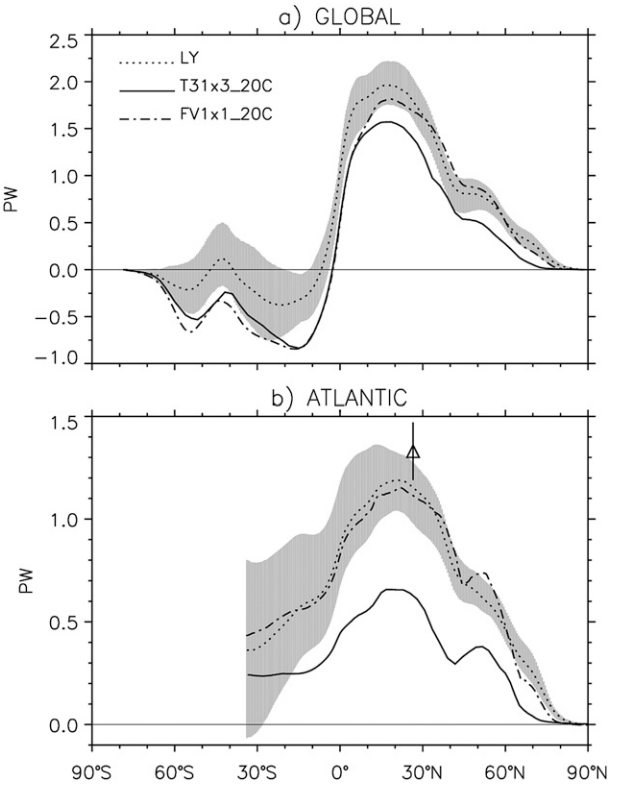

FIG. 15. (a) Global and (b) Atlantic Ocean northward heat transports. The global transports are the total transports and include the parameterized mesoscale, submesoscale, and diffusive contributions as well as the Eulerian-mean component; the Atlantic Ocean transports exclude the diffusive component. The dotted line denoted by LY represents implied time-mean transport calculated by Large and Yeager (2009) with shading showing the implied transport range in individual years. The triangle with the error bar is an estimate based on the RAPID data from Johns et al. (2011).

those of the higher resolution versions. In the Pacific Ocean, the Equatorial Undercurrent compares favorably with the Johnson et al. (2002) observations with both its maximum zonal speed (100 cm s^{-1}) and the depth and upward tilt from west to east of its core (not shown). Finally, compared to observations, while the mean SST is colder by 1°–2°C along the equatorial Pacific (Fig. 2), the SST seasonal cycle is in good agreement.

c. *The sea ice solution*

The quality of the modern sea ice simulation in the low-resolution CCSM4 is somewhat mixed. Overall, while the sea ice thickness and extent in the Southern Hemisphere are in agreement when compared to the sparse observations, the distribution of sea ice in the Northern Hemisphere is not correct. Figure 16 (top panels) shows a comparison of the winter (JFM) maximum ice area for the T31x3_20C and FV1x1_20C transient simulations for the period of 1986–2005 for the Northern Hemisphere. The black contours show the 10% concentration line from SSM/I satellite (Cavalieri et al. 1996) observations. The FV1x1_20C produces the best overall ice extent for the Arctic, while the T31x3_20C simulation is much too extensive. Jahn et al. 2012 found that, although FV1x1_20C produces the spatial distribution quite well compared to observations, ice thicknesses are still biased high. The JFM sea ice thicknesses in Fig. 16 (bottom panels) highlight the degradation in T31x3_20C. Part of the excessive thickness problem in the Arctic can be attributed to the turbulent mountain stress (TMS) parameterization, based on a sensitivity study without TMS, that produced ~20% less ice in the Arctic Ocean. Unfortunately, even without TMS, ice thicknesses were still too large. When developing the T31x3 model, we found that omitting ice runoff from land alleviates some

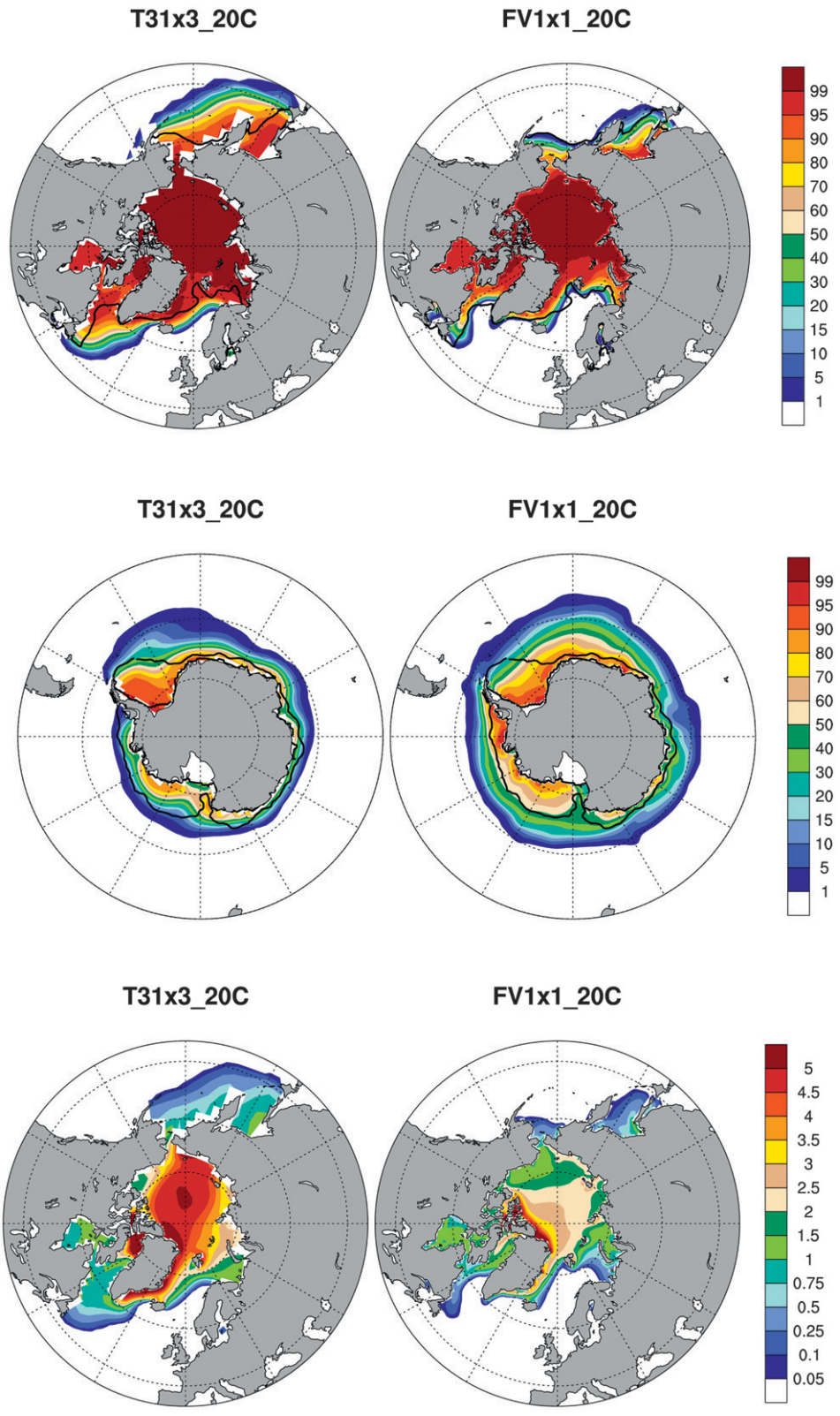

FIG. 16. (top) Northern Hemisphere JFM (boreal winter) sea ice fraction (%) for T31x3_20C and FV1x1_20C. (middle) Southern Hemisphere JFM (austral summer) sea ice fraction (%) for T31x3_20C and FV1x1_20C. (bottom) Northern Hemisphere JFM (boreal winter) sea ice thickness (m) for T31x3_20C and FV1x1_20C. SSM/I observations for sea ice (10% concentration) are shown with heavy black line for reference.

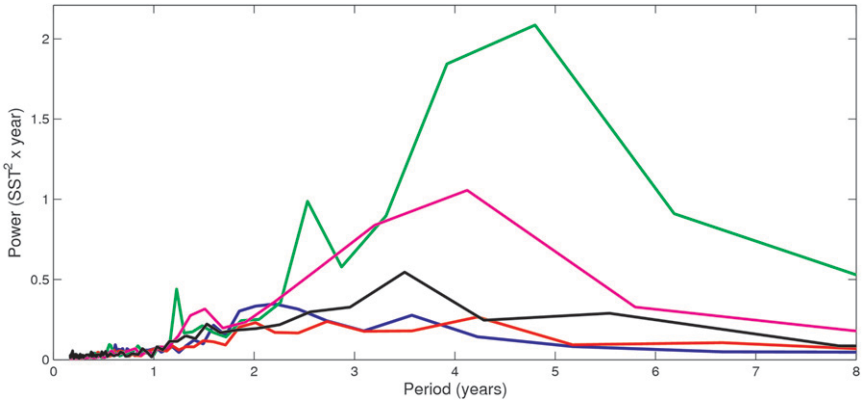

FIG. 17. Power spectrum for Niño-3 SST anomalies for HadSST (black), T31x3_1850 (blue), T31x3_20C (red), FV2x1_1850 (green), FV1x1_1850 (purple). The area under a line, when integrated across all periods, yields the total variance.

of the thickness bias in T31x3, particularly over the Baffin Bay region. Lowering inherent optical properties for snow on sea ice, that is, reducing the surface albedo, also helps to improve the overall thickness bias in the Arctic, but ultimately, even with these changes, all T31x3 simulations produce much too thick sea ice in the Arctic.

In the Southern Hemisphere (Fig. 16, middle panels), as in the 1850 control simulations, the summer (JFM) sea ice extent is greatly improved in the T31x3_20C simulation compared to the Northern Hemisphere. While both simulations are too extensive in summer compared to SSM/I satellite observations, the T31x3_20C produces a more reasonable ice extent compared to the higher resolution version.

We believe that the TMS parameterization does not have the same effect on the Southern Hemisphere as on the Arctic sea ice. In the Arctic, the TMS leads to much thicker sea ice in the central Arctic. By its nature, the TMS parameterization takes momentum from the equatorial region and moves it toward the pole. The excess momentum leads to a cooling of the polar regions. Hence the differing effects in the two hemispheres: In the south, the momentum is deposited over the continent and does not overly affect the Southern Ocean sea ice; while in the north, the excess momentum is deposited in the center of the Arctic Ocean, leading to substantial cooling and thicker sea ice. However, the benefits of turbulent mountain stress to the overall T31x3 model outweigh the detrimental effects on sea ice, hence TMS is applied by default to this configuration.

6. Climate variability

a. ENSO

The variability of ENSO on decadal to centennial time scales (e.g., Wittenberg 2009) requires us to provide a general circulation model for ENSO research that is fast, but realistic, and simulates the full set of relevant processes. In CCSM4 the modification of the convection scheme to account for convective plume dilution and convective momentum transport is a milestone for model development because it resulted in realistic ENSO periods and amplitudes (Neale et al. 2008). These improvements are realized in the coarse-resolution T31x3 as well (Jochum et al.2009), and the efficiency of this version allows for the rigorous statistical testing of ENSO hypotheses (Stevenson et al. 2010).

A detailed discussion of ENSO in the T31x3 resolution is beyond the scope of this brief overview, and the reader is referred to Jochum et al. (2010). The purpose here is merely to demonstrate that the recent release has realistic periods and amplitudes, too. The spectra are based on the Niño-3 SST (SST averaged over 5°S–5°N, 150°–90°W) for the years 201–500 in each of the control simulations and on the Niño-3 SST of the 130-yr Hadley Centre Global Sea Surface Temperature (HadSST) reconstruction (Rayner et al. 2006) for the observations (Fig. 17). The T31x3 simulations exhibit a broad spectrum of energy between 2 and 6 years as in the observations. This is true for the FV simulations as well, but the FV2x1 amplitude is excessive compared to observations. Thus, the new convection scheme does lead to realistic periods for all simulations, but does not seem to affect the amplitude of ENSO.

Purely kinematic arguments suggest that the ENSO amplitude has to depend on the zonal as well as vertical temperature gradient along the equator (e.g.; Schopf and Burgman 2006), but nonlinear feedbacks between SST and wind anomalies complicate the matter (e.g.; Gebbie et al. 2007). There are insufficient observations available to constrain the relative contribution of these processes [Capotondi et al. (2006) provides an

TABLE 1. Niño-3-mean SST (°C) and standard deviation of the seasonal cycle and the interannual variability.

Source	Mean	Seasonal cycle	Interannual variability
HadSST	25.7	0.95	0.79
T31x3_1850	24.0	1.08	0.65
T31x3_20C	24.1	1.03	0.69
FV2x1_1850	25.4	0.59	1.37
FV1x1_1850	25.4	0.72	1.02

exhaustive list], but it appears that anticorrelation between the strength of ENSO and of the seasonal cycle is a robust signal across all simulations (Table 1). We see that the relative strength of the seasonal cycle is a good predictor for the strength of ENSO, including observations, but that the mean SST is of little importance. By analyzing equatorial SST before and after the 1976 climate shift, this anticorrelation can actually be observed, and Guilyardi (2006) attributes it to the fact that, because ENSO is a disruption of the seasonal cycle, a weaker seasonal cycle is easier to be disrupted—and vice versa. This suggests that optimizing the simulated ENSO amplitude requires an improved simulation of the seasonal cycle.

b. NAM and SAM

Sea level pressure (SLP) and the Northern Annular Mode (NAM) in the T31x3 are comparable to the FV2x1. In the FV2x1, the strength of the North Atlantic winter low is too strong, whereas in T31x3 it is too weak. In the Southern Hemisphere the T31x3 has a slight high bias over the Antarctic continent (not shown).

To validate the NAM in T31x3, data from the last 26 years (1979–2005) of T31x3_20C are used to calculate the first empirical orthogonal function (EOF) of winter SLP (December–March). This time period was chosen to match observational records utilizing consistent and synchronous data across each separate data source. The principle components time series (PC1) are correlated against time series of surface temperature (TS) and precipitation rate (PRECT). Observational datasets are taken from the Hadley Center (SLP) (Allan and Ansell 2006), National Centers for Environmental Prediction (NCEP)–National Center for Atmospheric Research (NCAR) reanalysis (TS) (Kalnay et al. 1996), and Global Precipitation Climatology Project (GPCP) (PCP) (Yin et al. 2004) for years 1979–2008. To evaluate NAM in the control simulations, data (north of 20°N) was taken from the last 100 years of each experiment (T31x3_1850 and FV2x1_1850).

T31x3_20C captures the sea level pressure spatial variability and represents both major centers of action in the waters north of 60°N and over European continent. The shape and extent of the North Atlantic center of action, seen in Fig. 18, approximate observations, although the low-resolution model extends this feature more deeply into North America than exists in the observations. The obvious problem with the NAM, however, is a third center of action in central north Pacific, which is significantly larger when compared to observations. This ''tripole'' pathology has existed in all previous versions and resolutions of CCSM (Yeager et al. 2006) and CCSM4 is no different.

When analyzing the 1850 control experiments, the North Pacific feature appears to be much stronger in FV2x1_1850 and accounts for the largest variance in EOF1 sea level pressure, (Fig. 19). T31x3 and FV2x1 EOF1 sea level pressure exhibit different yet arguably equivalent errors in both shape and placement of NAM patterns. Correlations of sea level pressure PC1 to TS and PRECT (Fig. 18) show T31x3_20C capturing the key areas of temperature and precipitation anomalies across Europe and the Mediterranean region associated with NAM (Fig. 19).

The Southern Annular Mode (SAM) was also computed for the low-resolution control run, (not shown). T31x3 PSL variability over the Antarctic continent is much higher than observed. The FV2x1 does a better job at capturing shape and intensity of SLP EOF1 over the Antarctic as well as EOF1 correlation to sea ice extent and surface temperature. SAM was computed using annual SLP EOF1 across the last 50 years of the control simulations. NCEP records from 1979 to 2002 show 27% of the variance can be explained by SLP PC1 time series while this value for the T31x3_1850 and FV2x1_1850 simulations is 39% and 28%, respectively. Understanding why Antarctic sea ice and Southern Ocean climate compare well to observations while SAM is problematic is a subject for further study. A detailed analysis of sea level pressure in the context of the TMS parameterization is an obvious place to start, although the SAM problem appears to be more of a function of resolution rather than one with TMS. Spatial patterns of SAM and mean sea level pressure over Antarctica are not substantially different with or without TMS; in fact, including TMS reduces the mean SLP biases over Antarctica.

7. Climate sensitivity

The equilibrium climate sensitivity due to a doubling of CO_2 was assessed for the T31x3 model. This is accomplished by extracting implied horizontal and vertical oceanic heat transports and the mixed layer depths from the fully coupled control simulation. These forcing fields are then applied to a slab ocean model (SOM) formulation underneath fully active sea ice and atmosphere components (Bitz et al. 2012). Simulations were performed at

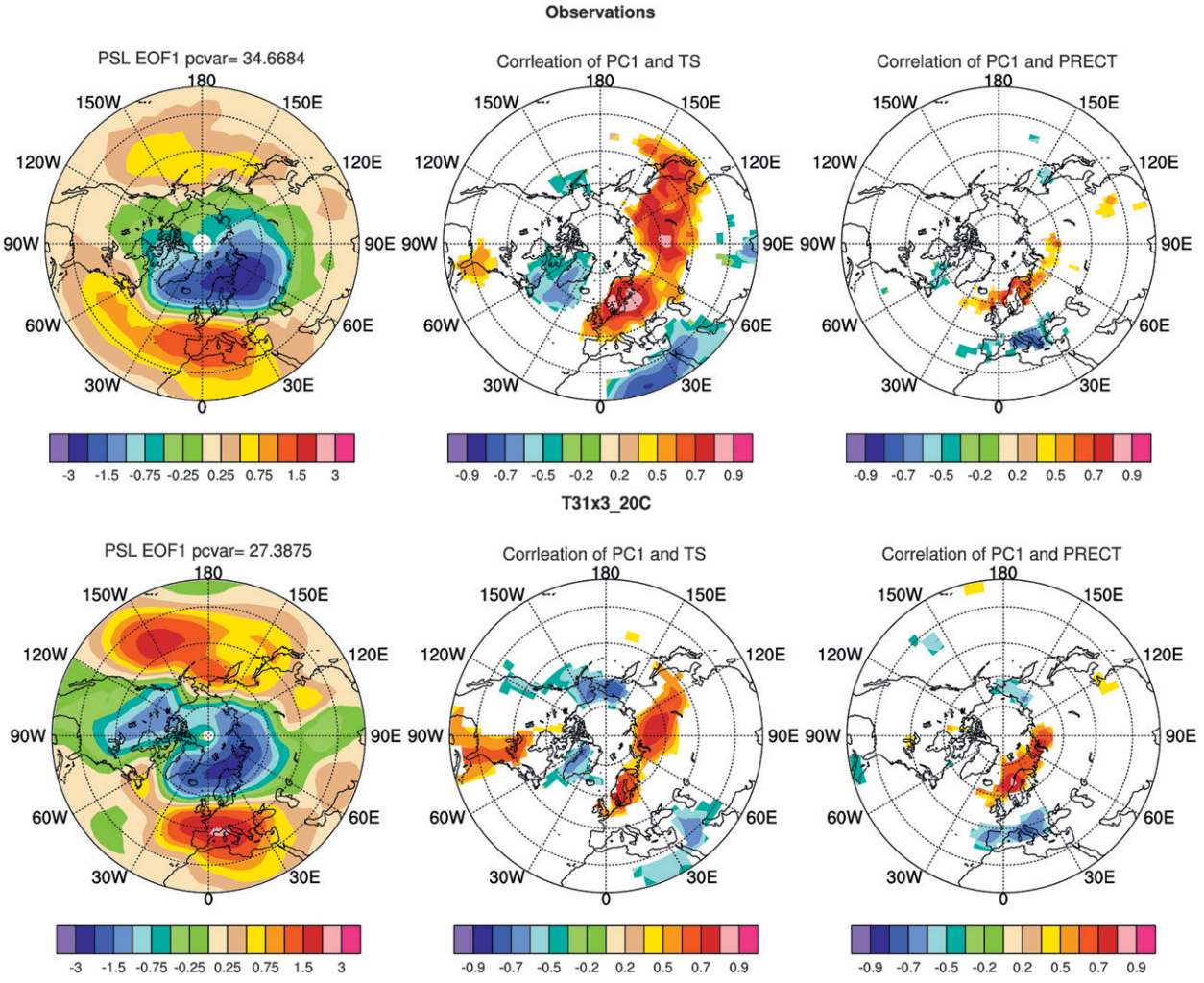

FIG. 18. The NAM analysis for (bottom) T31x3_20C vs (top) observations. (left) Winter [December–March (DJFM)] sea level pressure EOF1 and (middle and right) correlations to surface temperature and precipitation anomaly time series. Observations include the Hadley Center mean SLP dataset, NCEP mean monthly air temperature reanalysis, and GPCP precipitation and all use years 1979–2008. Model data matches the observational record for years 1979–2005. Correlations are plotted at the 95% significance level.

1850 CO_2 levels and double the 1850 level to assess the change in globally averaged surface temperature due to an instantaneous doubling of CO_2. By this definition, we found that the low-resolution CCSM4 has a climate sensitivity of 2.9°C, which is somewhat higher than its complement in CCSM3 (2.32°C) (Kiehl et al. 2006). The higher sensitivity of CCSM4 compared to CCSM3 is consistent across all resolutions of the model. As a detailed discussion of sensitivity and its resolution dependencies is beyond the scope of this paper, readers are encouraged to see Bitz et al. (2012) for an in-depth analysis of CCSM4 sensitivity.

8. Model performance

We have assessed the low-resolution CCSM4 performance on three platforms typically used to integrate the model. We have tried a variety of load balancing scenarios using Message Passing Interface (MPI) and Open MultiProcessing (OpenMP) parallelization. The model scales well over a fairly wide range of processor counts (Table 2). The best tested performance is 72 simulation years per actual (wallclock) day value on the National Center for Atmospheric Research's IBM Power6 with 192 processors (pes) and a total cost of 32 pe-hours/model year. By contrast, the FV2x1 model simulates approximately 15 simulation years per (wallclock) day with the same amount of processors. However, it should be noted that the optimal configuration for FV2x1 on the IBM Power6 utilizes 576 processors, which produces a throughput of 35 simulated years per (wallclock) day with a total cost of 200 pe-hours/model year. T31x3 is approximately six times less expensive

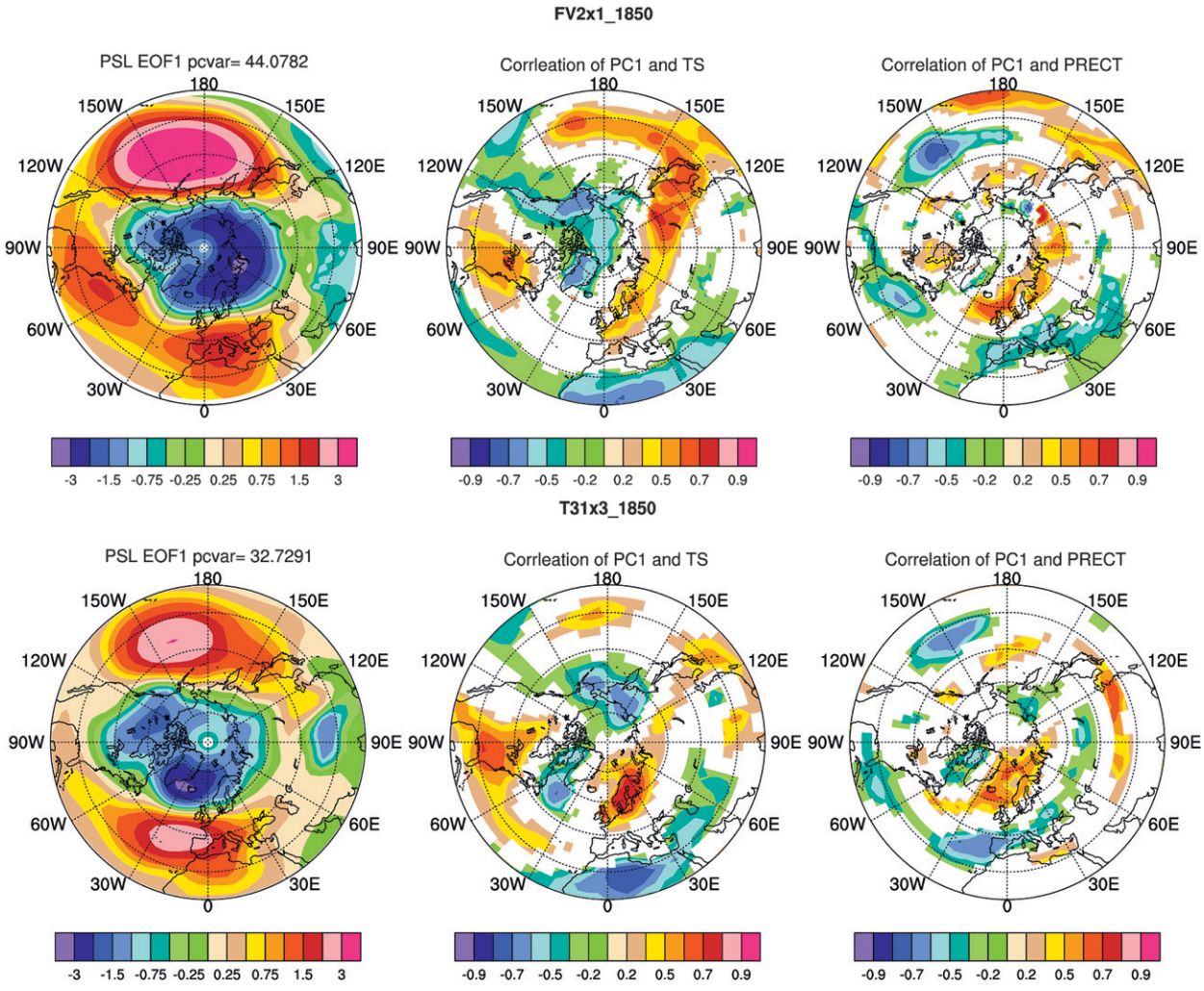

FIG. 19. The NAM analysis for (bottom) T31x3_1850 vs (top) FV2x1_1850. (left) Winter (DJFM) sea level pressure EOF1 and (middle and right) correlations to surface temperature and precipitation anomaly time series. The model data uses the last 100 years of time series in simulation. Correlations are plotted at the 95% significance level.

than FV2x1 when running with respective optimal configurations. Other CCSM4-supported machines include Linux clusters as well as the Cray XT4. We can achieve almost 20 years per day on the NCAR Linux cluster (Intel CentOS) with 64 processors and ~64 years per day on the National Energy Research Scientific Computing Center (NERSC) Cray XT4 with 420 processors.

Data volume is another consideration when resources are limited. In its default configuration, the low-resolution CCSM4 produces approximately 1.9 Gbytes/simulated year of data. The intermediate resolution produces ~16.6 Gbytes/simulated year and the standard resolution produces ~19.7 Gbytes/simulated year. Of course, data volume can be controlled within the model by limiting model history variables and frequency of output. Owing to the wide range of model configurations (resolutions and model components), supported machines, and potential processor configurations, we direct further inquiry on CCSM4 model performance and data volume statistics to the Community Earth System Model web site (available online at http://www.cesm.ucar.edu/models/ccsm4.0).

9. Discussion and summary

The low-resolution version of CCSM4 can be an alternative to the intermediate version of the model for most applications where cost is an issue. Long equilibrium runs, sensitivity experiments requiring numerous simulations, and model development projects are examples of science problems that require many simulation years. T31x3 is in agreement with both the observational

TABLE 2. Low-resolution (T31x3) CCSM4 performance on three typical platforms: an IBM Power 6; a Cray XT4; and a small Linux cluster. Top performance for each machine is highlighted in bold text. **FV2x1 and FV1x1 comparison figures are shown in italics. Note that T31x3 is not optimized for 512 or 576 pes.*

Machine	Processors (PES)	Simulated years/wallclock day	Total cost (PE-hours/simulated year)
CRAY XT4	**420**	**64**	**157**
CRAY XT4	220	54	98
CRAY XT4	120	41	70
Linux cluster	**64**	**19**	**80**
Linux cluster	48	18	66
Linux cluster	32	16	47
Linux cluster	16	10	38
IBM Power 6	576	**FV2x1: 35*	**FV2x1: 200*
IBM Power 6	512	**FV1x1: 13*	**FV1x1: 459*
IBM Power 6	**192**	**72,** **FV2x1: 15*	**32,** **FV2x1: 159*
IBM Power 6	128	49	31
IBM Power 6	64	32	24

twentieth-century temperature anomaly record and FV1x1-simulated anomalies. FV2x1 twentieth-century temperature anomalies are higher than both observations and other resolutions. Precipitation patterns for T31x3 across the globe are similar to that of FV2x1 and FV1x1 in that major biases, such as the double ITCZ, exist in all resolutions. Analysis of river transport as a metric to approximate the accuracy of the model water balance, in particular precipitation and river runoff, show the T31x3 model to approximate the FV2x1 in the Pacific basin and perform better in the Atlantic and Indian Ocean basins. The AMOC remains robust in the T31x3, although mixed layer depths remain too shallow in the North Atlantic. Maximum zonal wind stress magnitude for the Southern Hemisphere appears more in line with observational estimates than in the higher resolutions, although the storm track in the low-resolution model is displaced equatorward. This equatorial shift in the zonal surface stress in the Southern Hemisphere is a reflection of the Southern Hemisphere jet bias in the atmosphere and may have implications for Southern Ocean studies. The 500-hPa geopotential height is an improvement upon the FV2x1 in the Pacific Northwest, although biases still exist in the Arctic. The T31x3 model has a significant cold bias compared to the higher resolutions and observations. Low northward heat transport and cold surface temperatures, particularly in northern Arctic locales, lead to thick and extensive amounts of sea ice. The T31x3 Antarctic sea ice solution, however, is in agreement with observational records, in part, owing to improved wind stress.

Climate variability was also evaluated by analyzing ENSO, NAM, and SAM. T31x3 simulates the amplitude and period of ENSO events realistically compared to observations. Although the FV2x1 ENSO yields realistic periods as well, amplitudes are too large. The discrepancy in amplitude between T31x3 and FV2x1, however, is likely due to the implementation of the TMS parameterization in T31 CAM rather than a function of resolution. The NAM in T31x3 does not degrade with lower resolution and produces realistic statistics associated with this mode of variability. The SAM variability, however, is simulated more realistically with the FV2x1 and does show improvement with higher resolution.

Aside from the issues stated in this paper, the climate of T31x3 does not significantly degrade from the climate of FV2x1 but is a faster and more economical model. T31x3 can be considered a useful tool for experiments and projects that require many simulation hours. It is nearly five times faster than FV2x1 when running with the same number of nodes and processors on a supercomputer, yet flexible enough to work on a much smaller Linux machine with far less computing power.

Acknowledgments. NCAR and CCSM are sponsored by the National Science Foundation (NSF). We thank all CCSM scientists and software engineers for their hard work in developing and maintaining CCSM4. In particular, we thank the software engineering group for their technical support as well as the CCSM co-chair group for their willingness to spend the time necessary to present the best possible model to the community. We would also like to thank Andy Mai for his efficiency in completing the low-resolution twentieth-century simulation and three anonymous reviewers for their helpful comments. This research was supported by the National Science Foundation; the Office of Science (BER), U.S. Department of Energy (Shields), NSF SGP program (Shields), and NSF OPP 0908675 (Bailey). Computing resources were provided by the Climate Simulation Laboratory at NCAR's Computational and Information Systems Laboratory (CISL), sponsored by NSF and other agencies. This research was enabled by CISL compute and storage resources. Bluefire, a 4064-processor IBM Power6 resource with a peak of 77 TeraFLOPS provided more than 7.5 million computing hours, the GLADE high-speed disk resources provided 0.4 PetaBytes of dedicated disk, and CISL's 12-PB HPSS archive provided over 1 PetaByte of storage in support of this research project.

REFERENCES

Allan, R. J., and T. J. Ansell, 2006: A new globally complete monthly historical gridded mean sea level pressure dataset (HadSLP3): 1850–2004. *J. Climate,* **19,** 5816–5842.

Bitz, C. M., M. M. Holland, E. C. Hunke, and R. E. Moritz, 2005: Maintenance of the sea ice edge. *J. Climate,* **18,** 2903–2921.

——, K. M. Shell, P. R. Gent, D. Bailey, G. Danabasoglu, K. C. Armour, M. M. Holland, and J. T. Kiehl, 2012: Climate sensitivity in the Community Climate System Model, version 4. *J. Climate,* **25,** 3053–3070.

Boville, B. A., 1991: Sensitivity of simulated climate to model resolution. *J. Climate,* **4,** 469–485.

——, and P. R. Gent, 1998: The NCAR Climate System Model, version 1. *J. Climate,* **11,** 1115–1130.

Brohan, P., J. J. Kennedy, I. Harris, S. F. Tett, and P. D. Jones, 2006: Uncertainty estimates in regional and global observed temperature changes: A new dataset from 1850. *J. Geophys. Res.,* **111,** D12106, doi:10.1029/2005JD006548.

Capotondi, A., A. Wittenberg, and S. Masina, 2006: Spatial and temporal structure of tropical Pacific interannual variability in 20th century coupled simulations. *Ocean Modell.,* **15,** 274–298, doi:10.1016/j.ocemod.2006.02.004.

Cavalieri, D., C. Parkinson, P. Gloersen, and H. J. Zwally, 1996: Sea ice concentrations from Nimbus-7 SMMR and DMSP SSM/I passive microwave data. National Snow and Ice Data Center, Boulder, CO, digital media. [Available online at http://nsidc.org/data/nsidc-0051.html.]

Collins, W. D., and Coauthors, 2006: The Community Climate System Model, version 3 (CCSM3). *J. Climate,* **19,** 2122–2161.

Cunningham, S. A., S. G. Alderson, B. A. King, and M. A. Brandon, 2003: Transport and variability of the Atlantic Circumpolar Current in Drake Passage. *J. Geophys. Res.,* **108,** 8084, doi:10.1029/2001JC001147.

——, and Coauthors, 2007: Temporal variability of the Atlantic meridional overturning circulation at 26.5°N. *Science,* **317,** 935–938, doi:10.1126/science.1141304.

Dai, A., and K. E. Trenberth, 2002: Estimates of freshwater discharge from continents: Latitudinal and seasonal variations. *J. Hydrometeor.,* **3,** 660–687.

Danabasoglu, G., 1998: On the wind-driven circulation of the uncoupled and coupled NCAR climate system ocean model. *J. Climate,* **11,** 1442–1454.

——, W. G. Large, and B. P. Briegleb, 2010: Climate impacts of parameterized Nordic Sea overflows. *J. Geophys. Res.,* **115,** C11005, doi:10.1029/2010JC006243.

——, S. Bates, B. P. Briegleb, S. R. Jayne, M. Jochum, W. G. Large, S. Peacock, and S. G. Yeager, 2012: The CCSM4 ocean component. *J. Climate,* **25,** 1361–1389.

Gebbie, G., I. Eisenman, A. Wittenberg, and E. Tziperman, 2007: Modulation of westerly wind bursts by sea surface temperature: A semistochastic feedback for ENSO. *J. Atmos. Sci.,* **64,** 3281–3295.

Gent, P. R., S. G. Yeager, R. B. Neale, S. Levis, and D. A. Bailey, 2010: Improvements in a half degree atmosphere/land version of the CCSM. *Climate Dyn.,* **34,** 819–833, doi:10.1007/s00382-009-0614-8.

——, and Coauthors, 2011: The Community Climate System Model version 4. *J. Climate,* **24,** 4973–4991.

Guilyardi, E., 2006: El Niño–mean state–seasonal cycle interactions in a multi-model ensemble. *Climate Dyn.,* **26,** 329–348, doi:10.1007/s00382-005-0084-6.

Hack, J., J. Caron, G. Danabasoglu, K. Oleson, C. Bitz, and J. E. Truesdale, 2006: CCSM–CAM3 climate simulation sensitivity to changes in horizontal resolution. *J. Climate,* **19,** 2267–2289.

Holland, M. M., and M. N. Raphael, 2006: Twentieth century simulation of the Southern Hemisphere climate in coupled models. Part II: Sea ice conditions and variability. *Climate Dyn.,* **26,** 229–245.

——, D. A. Bailey, B. P. Briegleb, B. Light, and E. Hunke, 2012: Improved sea ice shortwave radiation physics in CCSM4: The impact of melt ponds and aerosols on Arctic sea ice. *J. Climate,* **25,** 1413–1430.

Hunke, E. C., and W. H. Lipscomb, 2008: CICE: The Los Alamos sea ice model user's manual, version 4. Los Alamos National Laboratory Tech. Rep. LA-CC-06-012, 76 pp.

Hurrell, J. W., J. J. Hack, D. Shea, J. M. Caron, and J. Rosinski, 2008: A new sea surface temperature and sea ice boundary dataset for the Community Atmosphere Model. *J. Climate,* **21,** 5145–5153.

Jablonowski, C., and D. L. Williamson, 2006: A baroclinic instability test case for atmospheric model dynamical cores. *Quart. J. Roy. Meteor. Soc.,* **132,** 2943–2976.

Jahn, A., and Coauthors, 2012: Late–twentieth-century simulation of Arctic sea ice and ocean properties in the CCSM4. *J. Climate,* **25,** 1431–1452.

Jochum, M., G. Danabasoglu, M. Holland, Y.-O. Kwon, and W. G. Large, 2008: Ocean viscosity and climate. *J. Geophys. Res.,* **113,** C06017, doi:10.1029/2007JC004515.

——, B. Fox-Kemper, P. H. Molnar, and C. Shields, 2009: Differences in the Indonesian seaway in a coupled climate model and their relevance to Pliocene climate and El Niño. *Paleoceanography,* **24,** PA1212, doi:10.1029/2008PA001678.

——, S. Yeager, K. Lindsay, K. Moore, and R. Murtugudde, 2010: Quantification of the feedback between phytoplankton and ENSO in the Community Climate System Model. *J. Climate,* **23,** 2916–2925.

Johns, W. E., and Coauthors, 2011: Continuous, array-based estimates of Atlantic Ocean heat transport at 26.5°N. *J. Climate,* **24,** 2429–2449.

Johnson, G., B. Sloyan, W. Kessler, and K. McTaggart, 2002: Direct measurements of upper ocean currents and water properties across the tropical Pacific during the 1990s. *Prog. Oceanogr.,* **52,** 31–61.

Kalnay, E., and Coauthors, 1996: The NCEP/NCAR 40-Year Reanalysis Project. *Bull. Amer. Meteor. Soc.,* **77,** 437–471.

Kiehl, J. T., C. A. Shields, J. J. Hack, and W. D. Collins, 2006: The climate sensitivity of the Community Climate System Model version 3 (CCSM3). *J. Climate,* **19,** 2584–2596.

Klinker, E., and P. D. Sardeshmukh, 1992: The diagnosis of mechanical dissipation in the atmosphere from large-scale balance requirements. *J. Atmos. Sci.,* **49,** 608–627.

Large, W. G., and S. G. Yeager, 2009: The global climatology of an interannually varying air-sea flux data set. *Climate Dyn.,* **33,** 341–364, doi:10.1007/s00382-008-0441-3.

Lawrence, D. M., K. W. Oleson, M. G. Flanner, C. G. Fletcher, P. J. Lawrence, S. Levis, S. C. Swenson, and G. B. Bonan, 2012: The CCMS4 land simulations, 1850–2005: Assessment of surface climate and new capabilities. *J. Climate,* **25,** 2240–2260.

Levitus, S., T. Boyer, M. Conkright, D. Johnson, T. O'Brien, J. Antonov, C. Stephens, and R. Garfield, 1998: *Introduction.* Vol. I, *World Ocean Database 1998,* NOAA Atlas NESDIS 18, 346 pp.

Lin, S. J., 2004: A ''vertically lagrangian'' finite-volume dynamical core for global models. *Mon. Wea. Rev.,* **132,** 2293–2307.

Matsuura, K., and C. J. Willmott, cited 2009: Terrestrial air temperature: 1900-2008 gridded monthly time series, version 2.01. [Available online at http://climate.geog.udel.edu/~climate/.]

Milton, S. F., and C. A. Wilson, 1996: The impact of parameterized subgrid-scale orographic forcing of systematic errors in a global NWP model. *Mon. Wea. Rev.,* **124,** 2023–2045.

National Oceanic and Atmospheric Administration, cited 2006: ETOPO2v2: 2-Minute Gridded Global Relief Data. [Available online at http://www.ngdc.noaa.gov/mgg/fliers/06mgg01.html.]

Neale, R. B., J. H. Richter, and M. Jochum, 2008: The impact of convection on ENSO: From a delayed oscillator to a series of events. *J. Climate,* **21,** 5904–5924.

Otto-Bliesner, B. L., E. C. Brady, and C. A. Shields, 2002: Late Cretaceous ocean: Coupled simulations with the National Center for Atmospheric Research Climate System Model. *J. Geophys. Res.,* **107,** 4019, doi:10.1029/2001JD000821.

Rayner, N. A., P. Brohan, D. E. Parker, C. K. Folland, J. J. Kennedy, M. Vanicek, T. Ansell, and S. F. B. Tett, 2006: Improved analyses of changes and uncertainties in sea surface temperature measured in situ since the mid-nineteenth century: The HadSST2 dataset. *J. Climate,* **19,** 446–469.

Schopf, P. S., and R. J. Burgman, 2006: A simple mechanism for ENSO residuals and asymmetry. *J. Climate,* **19,** 3167–3179.

Smith, R., and Coauthors, 2010: The Parallel Ocean Program (POP) reference manual, ocean component of the Community Climate System Model (CCSM). LANL Tech. Rep. LAUR-10-01853, 141 pp.

Steele, M., R. Morley, and W. Ermold, 2001: PHC: A global ocean hydrography with a high-quality Arctic Ocean. *J. Climate,* **14,** 2079–2087.

Stevenson, S., B. Fox-Kemper, M. Jochum, Rajagopalan, S. Yeager, 2010: ENSO model validation using wavelet probability analysis. *J. Climate,* **23,** 5540–5547.

Uttal, T., and Coauthors, 2002: Surface heat budget of the Arctic Ocean. *Bull. Amer. Meteor. Soc.,* **83,** 255–276.

Williamson, D. L., J. T. Kiehl, and J. J. Hack, 1995: Climate sensitivity of the NCAR Community Climate System Model (CCM2) to horizontal resolution. *Climate Dyn.,* **11,** 377–397.

Wittenberg, A. T., 2009: Are historical records sufficient to constrain ENSO simulations? *Geophys. Res. Lett.,* **36,** L12702, doi:10.1029/2009GL038710.

Yeager, S. G., C. A. Shields, W. G. Large, and J. J. Hack, 2006: The low-resolution CCSM3. *J. Climate,* **19,** 2545–2566.

Yin, X., A. Gruber, and P. Arkin, 2004: Comparison of CPCP and CMAP merged guage–satellite monthly precipitation products for the period 1970–2001. *J. Hydrometeor.,* **5,** 1207–1222.